Uptake of gaseous thallium, tellurium, vanadium and molybdenum into anhydrous alum, Lascar volcano fumaroles, Chile

N. Sainlot, I. Vlastélic, Séverine Moune, E.F. Rose-Koga, Federica Schiavi, S. Valade, F. Aguilera

*Manuscript

Uptake of gaseous thallium, tellurium and vanadium into anhydrous alum, Lascar volcano fumaroles, Chile

N. Sainlot[1,*], I. Vlastelic[1], S. Moune[1,2], E.F. Rose-Koga[1], F. Schiavi[1], S. Valade[1], F. Aguilera[3,4]

[1] Université Clermont Auvergne, CNRS, IRD, OPGC, Laboratoire Magmas et Volcans, F-63000 Clermont-Ferrand, France

[2] Observatoire volcanologique et sismologique de la Guadeloupe, Institut de Physique du Globe, Sorbonne Paris-Cité, CNRS UMR 7154, Université Paris Diderot, Paris, France

[3] Núcleo de Investigación en Riesgo Volcánico - Ckelar Volcanes, Universidad Católica del Norte, Avenida Angamos 0610, Antofagasta, Chile

[4] Departamento de Ciencias Geológicas, Universidad Católica del Norte, Avenida Angamos 0610, Antofagasta, Chile

* Corresponding author :

natacha.sainlot@uca.fr

(33) 4 73 34 67 39

Word count: 7978 (text body)

Abstract

Formation of secondary sulphate minerals during the reaction between volcanic gases and rocks modulates the composition and flux of gaseous emanations. We report on the sub-surface formation of anhydrous alum ($M^{I}M^{III}(X^{VI}O_4)_2$ with M^{I} = NH_4^+, Na^+, K^+; M^{III} = Al^{3+}, Fe^{3+} and X^{VI}= S^{6+}) in the 330°C fumaroles of the Lascar volcano (Chile). The alum occurs as a few millimetres thick crust that grew internally by two-way diffusion of reaction gases and diffusive influx of rock cations within the crust. The average growth rate is estimated at ca. 0.3 μm/day, based on the 19-year-long activity of the degassing fracture hosting the crust. The growth rate is controlled by the slow migration of the rock cations and decreases towards crust rim.

The crust selectively concentrates Tl, V and Te (thousands of μg/g) and to a lesser extent Mo (hundreds of μg/g). The uptake of gaseous Tl, V and Mo is not due to saturation of the gas with Tl, V and Mo compounds but to the possibility for the elements to enter the crystal structure of alum: Tl^+, V^{3+} and Mo^{6+} might substitute for the M^{I}, M^{III} and X^{VI} ions, respectively. The process of Te uptake remains uncertain, but must be related to the incorporation of Tl and V with which Te tightly correlates.

Thallium, V and Te concentrations increase by a factor > 20 from core to rim, where they reach 8760, 8508, and 1687 μg/g respectively. This trend correlates with the decrease of crust growth rate. This indicates that the low rate of rock cations supply to the outer edge of the crust favours the substitution of Tl, V and Te in the crystal network. Such surface enrichment does not occur for Mo, because Mo competes with S, another element from the gas. This suggests that the surface of mature alum crust has a high adsorption capacity for those gaseous metals able to compensate for the lack of rock-derived cations.

Based on the composition of gases escaping from the fracture hosting the crust, it is estimated that the partition coefficients of Tl (3.3×10^7), V (1.1×10^7) and Te (0.6×10^7) between crust surface and gases are two to four orders of magnitude higher than for other volatile metals and metalloids. It follows that gases equilibrating with anhydrous alums lose between 77 and 95% of their initial Tl content, but less than 1% of Pb. Given the Tl emission rate of Lascar volcano (5 g/day), between 17 and 104 g of toxic Tl would deposit every day if all Lascar gases were to equilibrate with anhydrous alums.

1. INTRODUCTION

Sub-aerial degassing of high-temperature magmas directly releases large amount of sulfur, metals and metalloids to the atmosphere (e.g., Allard et al., 2000; Moune et al., 2010; Mather et al, 2012; Zelenski et al., 2013; Gauthier et al., 2016). Conversely, gases continuously emanating from the crustal magma reservoirs feeding stratovolcanoes have a more complex history, and only a fraction escapes from the ground. The other fraction is trapped within the volcanic edifices, due to the dissolution of magmatic gases into groundwater (Doukas and Gerlach, 1995) and/or hydrothermal system (Symonds et al., 1992), formation of secondary sulphate minerals during gas-rock reactions (Zimbelman et al., 2005), condensation of sulpho-salt melts during gas expansion in fractures (Henley and Berger, 2013) and precipitation of gas sublimates at fumaroles vents as gas cools and mixes with air (Bunsen 1851; Stoiber and Rose, 1974). The extent of element uptake in the ground has implications for volcano monitoring (Symonds et al., 2001; Le Guern et al., 1993), and also controls the global versus local environmental impact of magmatic gases, especially regarding toxic heavy metals.

Several studies have collected gas sublimates and condensates at the mouth of fumaroles to document the condensation sequence of elements (e.g., Bernard and Le Guern, 1986; Symonds et al., 1987; Taran et al., 2001). In agreement with thermochemical data, they showed that semi-volatile elements (Cd, Pb, Bi, Cu, Zn) condense over a wide temperature range, from 800 to less than 400°C, depending on gas composition and oxidation state (e.g., Symonds et al., 1987; Le Guern et al., 1993; Churakov et al., 2000). Fewer studies noted that fumarolic incrustations are also enriched in some volatile metals (e.g. Cu, Tl) that are not saturated in the gas phase (Naughton et al., 1976; Kodosky and Keskinen; 1990; Okrugin et al. 2017). They suggested that gaseous elements partition into, or adsorb on the alteration minerals coating degassing conduits. There is growing evidence that underground gas-rock reactions significantly influence the chemistry of volcanic gases ultimately released in the atmosphere (Henley and Berger, 2013; Henley and Seward, 2018; King et al., 2018; Palm et al., 2018). For instance, Henley et al. (2012) emphasized the fractionation of chalcophile elements (As-Sb-Bi-Sn-Pb-Tl) during sub-surface precipitation of sulpho-salts and suggested that over 90% of As might be trapped underground.

This study focuses on the partitioning of gaseous elements into secondary sulphates, which commonly form when acid gases interact with basaltic or more evolved rocks rich in aluminium and alkalis (Getahun et al., 1996; Africano and Bernard, 2000; Zimbelman et al., 2005). The range of secondary sulphate minerals is wide due to the numerous possibilities of combining rock-derived cations (K^+, Na^+, Ca^{2+}, Mg^{2+}, Al^{3+}, Fe^{3+}) with gas-derived ions (NH_4^+, SO_4^{2-}). In addition, trace ions with valence ranging from +1 to +6 might substitute for major cations, further increasing mineral variety (Lipson et al., 1935; Giester, 1994; Balic Zunic et al. 1994; Dutrizac and Jambor, 2000). For instance, more than one hundred of sulphate minerals occur in the fumarolic incrustations of Tolbachik volcano, Kamchatka (Mindat.org database, 2019).

The geochemical study of gas-rock interaction meets with the difficulty of accessing the active areas of stratovolcanoes and collecting underground samples. To circumvent this difficulty, Henley et al. (2012) studied paleo-fumarole conduits, now exposed at the surface by tectonics. Here, we use a sub-surface fumarole crust showing growth layers to reconstruct the temporal evolution of the gas-rock reaction within a degassing fracture of the Lascar volcano (Chile). This evolution is studied by measuring in situ major-trace element concentrations and oxygen isotopes along core-rim profiles. The bulk Pb and Sr isotopic composition of the crust is also measured to constrain the origin of the crust. The composition of the outermost layer of the crust is compared to the composition of gases emanating from the same fracture (Menard et al., 2014), in order to assess the partition coefficients of elements between gas and crust. A major result of this study is the recognition of selective incorporation of gaseous Tl, V and possibly Te in the crystal structure of the sulphate. This effect potentially depletes volcanic emanations in these elements and contributes to concentrate them within the edifice.

2. BRIEF OVERVIEW OF LASCAR VOLCANO

Lascar (23°22'S, 67°44'W, 5590m) is one of the most active stratovolcanoes of the Central Volcanic Zone (CVZ) of the Andes (Fig. 1a) (Stern, 2004). The volcano rests on a pre-Cenozoic basement, made of Devonian to early Carboniferous sandstones (Lila formation), Permian granites and volcanic rocks (Cas formation), Permo-Trias volcanic products (Peine strata and Cerro Negro Strata) (Gardeweg et al., 1998, 2011). The volcano is composed of two cones, the westernmost crater of the eastern edifice being

the current focus of activity (Fig. 1b). The volcano has produced about 30 to 40 km^3 of magma during its 220 ka history. Since the nineteenth century Lascar produced ca. 30 eruptions andesitic-to-dacitic in composition (Gardeweg et al., 1998, 2011). Petrochemical modelling indicates the occurrence of large magmatic reservoir at 6 km depth, which is mobilized during dacitic eruptions, and several shallower reservoirs sampled by smaller but more frequent mafic eruptions (Matthews et al., 1999). Between the 1984 reactivation and the last major eruption in 1993, Lascar showed a cyclic activity including sequences of dome growth, degassing pulse, dome subsidence, and explosive events (Matthews et al., 1997). The 1993 eruption (VEI 4) produced a 25 km-high sub-plinian ash column whose collapse generated pyroclastic flows up to 8.5 km NW from the summit. The eruption deposited 10^9 tons of tephra, coated by gypsum likely recycled from tertiary sediments (Risacher and Alonso, 2001). Since 1993, Lascar alternated passive degassing and vulcanian eruptions, and produced its last eruption in October 2015.

A major feature of Lascar volcano is the high fumarolic activity that feeds a persistent gas plume. Sampling of the active crater fumaroles between 2002 and 2006 revealed temperatures in the range of 30-385°C and the contribution of magmatic gases, hydrothermal fluids, and meteoric water to volcanic emanations (Tassi et al., 2009). The hottest fumaroles (250-385°C) occurred within a narrow area to the northeast of the active crater. Menard et al. (2014) sampled the gas plume between 2009 and 2012, and estimated that the volcano releases 150-940 t/d SO_2, 170-210 t/d HCl, and up to 100 t/d HF. They also identified little volatile (i.e., Co, V, Sc, REE, Y, HFSE, Th, U, alkali–earth and alkaline metals), moderately volatile (Cu, Cr, W, In, Mo, Sn, Pb), and highly volatile (Cd, Zn, B, Tl, Sb, Bi, Se, As, Te) groups of trace elements.

3. FUMAROLE CRUST SAMPLE

A fumarole crust was sampled in November 2012 in the arcuate fracture located along an older crater wall east of the active crater, at an elevation of 5375 m (Fig. 1b). This fracture opened following the 1993 eruption (Matthews et al., 1997). Gases emanating from the fracture were also sampled in 2012 through filter packs ca. 2m from the fracture (Fig. 2a) and analysed by Menard et al. (2014). The gases have a low SO_2/HCl molar ratio (0.21) compared to plume aerosols (average of 1.7) and fumaroles from the

active crater (average of 3.0) (Menard et al., 2014, Tassi et al., 2009). Such low SO_2/HCl ratio is indicative of extensive gas–water–rock interactions. The temperature of the bottom of the fracture where the crust formed, measured by thermal camera, was 330°C (Fig. 2b). This temperature is unexpectedly elevated given the distance from the active crater (ca. 500 m) and the hydrothermal signature of the gases.

The studied crust was attached to the lower surface of a lava block that obstructed the fracture (Fig. 2cd). It was collected ca. 30 cm underground. The crust was initially fully green, but some parts became blue a few minutes after sampling as the crust equilibrated with air. Crust colours faded during the first year that followed sampling. The crust coats the rock over ca. 100 cm^2 and is a few mm thick (Fig. 2d). It includes several outgrowths, more or less cracked and hollow (Fig. 2e). Inspection of different cross sections under a binocular microscope revealed that they formed via concentric addition of growth layers. A globular outgrowth, ca. 8 mm in diameter and filled with crust material was selected for this study (Fig. 2f).

4. METHODS

All analyses were done at Laboratoire Magmas et Volcans (LMV), Clermont-Ferrand, except Secondary Ion Mass Spectrometry (SIMS) measurements which were carried out at CRPG, Nancy.

4.1. Electron Microscopy

The selected crust chip was embedded in resin, polished on SiC discs using ethanol to preserve water-soluble phases. An area of 2.0×1.5 mm showing well-formed growth layers was selected for chemical analysis (Fig. 2f). All analyses, with the exception of oxygen isotopic composition, were performed on this reference area (referred to as side A). This area was first surveyed by Scanning Electron Microscopy (SEM, JSM 5910LV) operating in Backscattered Electron (BSE) imaging mode. Detected elements (S, O, Al, Fe, Mg, Na, Ca and K) were mapped by Energy Dispersive Spectroscopy (EDS). Quantitative analyses of major elements, with the exception of O, were subsequently performed by Electron Probe Microanalysis (EPMA, Cameca SX 100) along two core-rim profiles, referred to as A1 and A2 (location shown in Table S1), with a 15-kV accelerating voltage,

10-nA beam current, and 30μm spot size. Relative in-run errors (2σ) are typically 4% for Al and S, 12% for Fe, Mg and Na, 20% for K and 30% for Ca.

4.2. Laser ablation inductively coupled plasma mass spectrometry

Concentrations of minor and trace elements (Li, Sc, V, Cr, Co, Ni, Cu, Zn, Ga, Ge, As, Rb, Sr, Y, Zr, Nb, Mo, Cd, In, Sn, Sb, Te, Cs, Ba, Hf, Ta, Tl, Pb, Bi, Th, U and Rare Earth Elements) were measured on the EPMA spots by laser ablation inductively coupled plasma mass spectrometry (LA-ICPMS) using an excimer 193nm Resonetics M-50E laser system and an Agilent 7500cs quadrupole ICPMS. Measurements were done with a dwell time of 25 ms, spot size of 27 μm, laser repetition rate of 3 Hz, He and N_2 flow rates of 575 and 2 ml/min, respectively. Backgrounds were measured for 30s before each ablation. Oxide production as measured by ThO/Th on the NIST 610 standard glass was 0.9%. Aluminium content was used for internal normalization, with reference to EPMA data. The NIST 610 was measured several times at the beginning of the session and then every 25 spots. As no significant drift occurred, the average of the NIST 610 measurements were used for signal calibration, using the GeoRem database values (Jochum et al., 2005). Relative error on the NIST 610 is less than 1% for each measured trace elements. The GLITTER software was used for the trace-element data reduction. Detection limit was <1ppm for all elements except Se, which was measured by wet chemistry (cf. 4.5).

4.3 Raman spectroscopy

Raman spectroscopy was used to characterize crust mineralogy. Raman spectra were collected using an InVia confocal Raman micro-spectrometer manufactured by Renishaw and equipped with a 532 nm diode laser, a CCD detector, an edge filter, a motorized XYZ stage and a Leica DM 2500M optical microscope. Laser power on the sample was reduced to ~ 1 mW and slit aperture was set to 65 μm. A 50× microscope objective and a 2400 l/mm grating were used. Spectral resolution was better than 1 cm^{-1}. Daily calibration of the spectrometer was performed based on a Si 520.5 cm^{-1} peak. The spectra were recorded in the 60-1320 and 2920-3740 cm^{-1} wavenumber ranges using Wire 4.2 software.

4.4. Secondary Ion Mass Spectrometry

Following Raman analysis, the surface of the sample became crackled. A 1 mm-thick slice was sawed to perform oxygen isotope analysis by SIMS on the opposite side of the slice (referred to as side B). The use of a thin slice also limits degassing of the epoxy resin and of the hydrated sulphate sample within the mass spectrometer. Oxygen isotopes ($\delta^{18}O$) measurements were carried out with a SIMS 1270. The slice was coated with three 4nm-thick layers of gold to assure a good electrical conduction of the porous sample. The same protocol has been applied to standard samples. Oxygen isotope compositions were measured along 3 core-to-rim profiles in the same area as major-trace element analysis. Profile B1 and B3 were perpendicular, and profile B2 was in between profile 1 and 3 (locations reported in Table S2). The spot size was 15 µm and the distance between spots was 40µm in the first and the second profile, and 56.6 µm for the third profile.

The SIMS was set in multi-collection mode with ^{16}O, ^{17}O and ^{18}O isotopes counted in L2, H1 and axial faraday cups, respectively. The field aperture and MRP were set at 2000 and 6000, respectively. We applied a 30µm raster during the 120 s pre-sputtering, and a 25µm raster during data acquisition. The total analytical time for one measurement was 6 min. The calcite CCcigA reference material with $\delta^{18}O$ =18.94‰ ±0.14(2σ) (Pfister et al., 2018) was first repeatedly analysed in order to assure the SIMS measurements stability. Instrumental mass bias and drift were corrected by measuring at the beginning and at the end of each profile the composition of a sulphate standard with homogeneous and known isotopic composition (CRPG internal standard $BaSO_4$ from Maïza, with $\delta^{18}O$ of 14.45‰). The in-run error was on average 0.25‰ (2σ).

4.5. N, H, S and Se bulk analysis

Bulk concentrations of N, H, S and Se were measured on finely crushed surface scrapings. Nitrogen, H and S were analysed using a Flash 2000 CHNS-O elemental analyser from Thermo Fisher Scientific. Circa 1 mg of powder and a similar amount of V_2O_5 were precisely weighted in a tin capsule using a microbalance, and introduced into the 950°C high-temperature reactor. The combustion gases (N_2, H_20 and SO_2) were

separated in the coupled chromatography column and quantified by thermal conductivity. Cystine ($C_6H_{12}NO_4S_2$) was used for calibration. Selenium was measured by ICPMS after sample dissolution in 6M HCl, evaporation and dilution in 0.5M HNO_3.

4.6 Pb and Sr isotope bulk analysis

Four crust chips were powdered in an agate mortar. Circa 50 mg of sample were dissolved and Pb and Sr were extracted using anion exchange resin (AG1-X8) and Sr chelating resin (Sr Spec), respectively, following the methods described in Vlastelic et al. (2013). The isotopic compositions were measured on a Neptune Plus MC-ICPMS (Pb) and on a Triton TIMS (Sr). Instrumental mass bias correction is detailed in Table S3.

5. RESULTS

5.1. Crust mineralogy

Electron microscopy survey of the crust section shows a finely crystallized sulphate of Al, Fe, Na, Mg, K and Ca. Electron microprobe analyses performed along the two core-rim profiles A1 and A2 give between 19.5 and 23 wt% S, between 5.4 and 9.3 wt% Al, and between 0.5 and 4.2 wt% Fe (Table S1). Sodium ranges from 0.6 to 3.9 wt%, Mg from 0.7 to 3 wt% and K from 0.2 to 1.6 wt%. Calcium is generally less than 1 wt%, but frequent spikes (up to 8.5 wt%) occur due to the presence of anhydrite nuggets. Aluminium negatively correlates with Fe and Mg, whereas K negatively correlates with Na. Atomic abundances follow the relation: S/(Al+Fe)=0.16(Ca+Mg)+1.9, which is consistent with the occurrence of a double sulphate of Al and Fe.

Raman spectra (Fig. 3) show the characteristic vibration bands of (1) anhydrous alums, with major occurrence of $(NH_4)Al(SO_4)_2$ (godovikovite bands at 318, 483, 610 and 653, 1076, 1287, 3148, 3208, 3331 cm^{-1}), and minor occurrence of $(NH_4)Fe(SO_4)_2$ (sabieite main band at 1033 cm^{-1}) and $(NH_4)_2Mg_2(SO_4)_3$ (efremovite main band at 1049 cm^{-1}) (Kosek et al., 2018); (2) hydrated sulphates including $MgSO_4{\cdot}6H_2O$ (exahydrite bands at 460±5, 610, 983-984, 1080 and 3435 cm^{-1}), mirabilite ($Na_2SO_4{\cdot}10H_2O$) and/or hydrated alums (band at 990/991 cm^{-1}); and (3) $CaSO_4$ (anhydrite bands at 416, 499, 609, 627, 675, 1017 and 1129 cm^{-1}) (Frezzotti et al., 2012). The average K/Al atomic ratio of

0.10±0.05 (1σ) is consistent with minor occurrence of K in godovikovite (Shimobayashi et al., 2011). Bulk volatile element analysis in the surface scrapings yields 1.37-1.51 wt% N, 3.19-3.32 wt% H and 18.10-19.15 wt% S, which indicates relatively low proportion of godovikovite (<25 wt%) and high proportion of hydrated phases in the outer layer of the crust. Inspection of the unpolished surface of the crust by electron microscopy (Supplementary material S4) reveals the occurrence of 5-10 μm Te-rich crystals embedded within fine-grained Na_2SO_4. Once corrected for background Na, S and O (assuming all Na signal is from background Na_2SO_4) the composition of these crystals turns out to be TeO_2 with minor amount of S. Other surface minerals are anhydrite, quartz, Ba sulphate, and a Tl-rich Al sulphate whose composition cannot be precisely determined due to its very small size (ca. 1 μm).

5.2. Crust layering and compositional zonation

The SEM image of the crust section shows at least 11 concentric growth layers (U1-U11) whose thickness (500-30 μm) generally decreases towards crust rim (Fig. 4a). The growth layers do not have the same thickness in all directions indicating an anisotropic growth. Element mapping (Fig. 4b-d) shows that Al tends to increase towards the layer boundaries, the boundaries themselves being enriched in Fe. Anhydrite occurs as particles, whose number increases towards crust rim as their size decreases. Generally major elements do not show core-rim trends beyond a slight decrease of S and K, and increase of Na in the external shells (U1 to U3). The sum of the measured major elements, plus O, N and H calculated taking into account anhydrous minerals only (godovikovite, sabieite, efremovite and anhydrite) decreases from 90 to 80 wt.% from core to rim (Table S1). This indicates an increase of water content and/or porosity towards crust rim. The first possibility is supported by the 40% increase of the EDS oxygen signal from core to rim, and the elevated H content (>3 wt%) in the surface scrapings. It is not known whether the outer shell of the crust was initially hydrated, or hydrated between sampling (2012) and analysis (2014).

In situ trace element concentrations are reported in Table S1. Many trace elements commonly transported by magmatic gases (Pb, Bi, Zn, Cu, Cd, Sn, Rb) occur in the crust in concentrations that are similar to or lower than those of Lascar lavas, and do not show core-rim trends (Fig. 5). Tellurium, thallium and molybdenum stand out, with

concentrations between 4.10^2 and 10^7 times those of lavas (Fig. 5). Selenium, arsenic and vanadium show second order enrichments (between 22 and 37) principally at crust rim. Vanadium together with Tl and Te show a marked zonation across the crust, with concentrations increasing from 297, 210 and 71 ppm in crust core to 8508, 8760 and 1687 ppm at crust rim, respectively (Fig. 6a). This increase is the most pronounced near the rim of the crust, between U6 and U1, with a local high in layers U3-U4 (1897 ppm V, 2622 ppm Tl and 944 ppm Te). Molybdenum does not show such zonation, but slightly higher concentrations in the middle of the crust (600-924 ppm) compared to core and rim (205-710 ppm). Despite their large ranges of variation, Tl, V and Te are little fractionated from each other, with Tl/V=1.4±1.1(2σ), Tl/Te=3.6±2.7(2σ) and V/Te=2.9±2.4 (2σ) (Fig. 6b).

5.3. Oxygen isotope profiles

In situ $\delta^{18}O$ values measured along the three profiles of side B are reported in Table S2. $\delta^{18}O$ compositions calibrated with the $BaSO_4$ standard from Maïza show similar ranges of variation along B1 (-1.2 to +8.2‰), B2 (-1.6 to +5.4‰) and B3 (-2.2 to +6.4‰) profiles. These variations are clearly outside the errors of individual measurements, which do not exceed 0.4‰. $\delta^{18}O$ does not show systematic core-rim trend but high-frequency fluctuations (Fig. 7). Depending on the profile, $\delta^{18}O$ display between 12 and 20 oscillations that are not obviously linked to the growth layers. Profile B2 tends to show a smooth evolution of $\delta^{18}O$ between +2.5 and 5.4‰, on which superimpose low $\delta^{18}O$ spikes. The average $\delta^{18}O$ of the three profiles (+3.5 ±1.8 (σ), n=165) is identical to the composition of Lascar gas condensates (+3.5±1.2(σ) n=2) (Tassi et al., 2009). Thus, despite the small-scale heterogeneity of $^{18}O/^{16}O$ within the crust, no net isotopic fractionation occurs between vapour and the bulk sulphate crust.

5.4. Bulk Pb and Sr isotope composition

The bulk Pb and Sr isotope compositions of the four crust chips are reported in Table S3. The variations of $^{206}Pb/^{204}Pb$ (18.803-18.821), $^{207}Pb/^{204}Pb$ (15.648-15.661), $^{208}Pb/^{204}Pb$ (38.783-38.830), and $^{87}Sr/^{86}Sr$ (0.706329-0.706482) are small and identical, within error, to the composition of lavas from the 1993 eruption ($^{206}Pb/^{204}Pb$=18.817-18.819;

$^{207}Pb/^{204}Pb$=15.654-15.657; $^{208}Pb/^{204}Pb$=38.795-38.803; $^{87}Sr/^{86}Sr$=0.706337-0.706438) (Rosner et al. 2003).

6. DISCUSSION

This study investigates a time series of metal variations in a zoned sulphate crust that grew on a lava block continuously exposed to fumarole gas flux from Lascar volcano. The following discussion will focus on crust formation processes and time-scale, the extent of element extraction from the lava block relative to the gas flux, and the extensive uptake of V, Tl and Te from the gas phase.

6.1. Crust formation processes

Anhydrous alums frequently occur at the degassing vents of burning coal-dumps (BCDs) (see review by Kosek el al., 2018). There, godovikovite commonly forms stalactite or thick crusts in subsurface cavities. Anhydrous alums are less common in volcanic fumaroles: godovikovite has been described in the Phlegrean fields and La Fossa crater on the island of Vulcano (Mindat.org database, 2019), while its hydrated form (Tschermigite) has been found in the thermal fields of Southern Kamchatka Peninsula (Zhitova et al., 2019), East African rift (Lowenstern et al., 1999) and possibly Merapi volcano, Indonesia (Kavalieris, 1994). Steklite, $KAl(SO_4)_2$, the K-analogue of godovikovite, has been identified in the fumarole deposits of Tolbachik volcano, Kamchatka (Murashko et a., 2013). Godovikovite is stable between 210 and 390°C (Zhitova et al., 2019), in agreement with the temperature (330°C) of the Lascar degassing fracture where the studied crust was sampled. Godovikovite hydrates into an amorphous phase below 200°C, and into tschermigite below 60°C. Conversely, it loses ammonium above 380°C to form millosevichite (Zhitova et al., 2019). The occurrence of godovikovite throughout the crust indicates that the temperature has remained relatively stable during crust formation history. The suspected hydration of the outer shell of the sulphate crust is likely a post-formation process, as observed in a BCDs crust (Parafiniuk and Kruszewski, 2009).

Symonds et al. (1992) estimated that even under highly oxidizing conditions (fO_2 of 10^{-5}), sulphuric acid and its hygroscopic forms are undersaturated above 202 °C in a gas

with less than 0.01% moles S, i.e. more than 10 times the S content of Lascar gases (Tassi et al., 2009). Thus, the Lascar crust must have formed by the interaction between gases and silicate rocks. This happens either through the reaction between $SO_{3(g)}$ and silicate without change in S oxidation state, or through the disproportionation of $SO_{2(g)}$ to SO_4^{2-} that bonds with rock derived cations, and reduced S released as $S_{2(g)}$ or $H_2S_{(g)}$ (Henley et al., 2015; Renggli et al., 2018). Because this reaction requires diffusion of elements towards the gas-rock interface, sulphates of Ca, Na and to a lesser extent Mg preferentially form, while sulphates of less mobile networkforming cations (Al, Fe) are rarely observed in experiments (Renggli et al., 2018; King et al., 2018). For instance, anhydrite might form through chemisorption of $SO_{2(g)}$ on anorthite (Henley et al., 2015):

$$3CaAl_2Si_2O_8 + 4SO_{2(g)} + H_2O_{(g)} \rightarrow 3CaSO_4 + 3Al_2SiO_5 + 4SiO_2 + H_2S_{(g)} \quad (1)$$

Johnson and Burnett (1993) nevertheless reported the formation of a mixture K-Na anhydrous alum and thenardite following one week reaction at 850°C between crystalline albite ($NaAlSi_3O_8$) and a gas mixture with SO_2/O_2=1 obtained by thermal decomposition of $K_2S_2O_8$. This experiment demonstrates that, in oxidizing conditions, gas-derived (K and S) and silicate-derived (Na and Al) elements combine to form anhydrous alum. The layered structure of anhydrous alums, which results from stacking thin layers of $Al(SO_4)_2^-$ and layers of large cations (K^+, NH_4^+) (West et al., 2008; Murashko et a., 2013; Zhitova et a.l., 2019), suggests a two step formation process. One possibility is that the anion layer first forms by chemisorption of $SO_{2(g)}$ on residual silicate but is weakly bonded to H^+, allowing the sorption of larger species from the gas subsequently:

$$Al_2SiO_5 + 6SO_{2(g)} + H_2O_{(g)} \rightarrow 2[H^+Al(SO_4)_2^-] + S_{2(g)} + SiO_2 \quad (2)$$

$$[H^+Al(SO_4)_2^-] + NH_{3(g)} \rightarrow NH_4Al(SO_4)_2 \quad (3)$$

and generally, for any monovalent cation M^I transported as chloride in the gas,

$$[H^+Al(SO_4)_2^-] + M^ICl_{(g)} \rightarrow M^IAl(SO_4)_2 + HCl_{(g)} \quad (4)$$

The formation of godovikovite requires a sustained supply of gaseous NH_3. Nitrogen may originate from the devolatilization of sediments subducted into magmas source (Snyder et al., 2003) and/or unusually elevated nitrate concentration in Atacama terrains due to the hyperarid climate (Ericksen G., 1983).

After the initial stage of gas-rock interaction, growth of a sulphate crust requires transport of elements through the sulphate. Different growth textures will form depending on whether rock cations migrate towards the sulphate-gas interface, or gas-derived elements migrate towards the sulphate-silicate interface, or rock and gas elements both migrate within the sulphate. Renggli et al. (2018) studied the formation of anhydrite coating during short (24-72H) high-temperature (700-800°C) reaction between $SO_{2(g)}$ and Fe-free glass. They observed that the thickest coatings (ca. 200 μm) tend to detach from the glass surface and to wrinkle and buckle, which they ascribed to stress accumulation within the coating due to internal sulphate growth. They suggested that the empty space between the buckled coating and silicate substrate might fill with sulphate material in case of longer durations. The outgrowths of the Lascar crust very likely form via a similar process (Fig. 8ab), although the aluminous composition and thickness of the sulphate crust indicate that the extent of reaction is much higher. In particular, the prolonged gas-rock reaction results in the formation of growth layers. The layers are ascribed to a decreasing growth rate towards crust surface due to the slow diffusion of rock-cations within the altered rock and the sulphate. Element migration occurs through evolving vacancies, defects and grain boundaries, and is much less efficient for Al than for Ca, Na, Mg and other divalent cations (Henley et al., 2015; Palm et al., 2018). As the crust grows, the progressive exhaustion of cations in the reacted rock also requires cations to diffuse over longer distances. The thin layers at crust outer edge are consistent with a slow growth due to a low rate of rock cations supply. As shown on Figure 8c, the structure of the crust is consistent with a model where all layers grow simultaneously, but at decreasing rate towards the rim.

In the internal growth model, the small-scale $^{18}O/^{16}O$ variations across the crust have no temporal significance. They result from the stacking of the temporal O isotope signal of the gas. The substantial isotope variations nevertheless require the input of sources with different compositions, such as meteoric water with $\delta^{18}O$ of -19‰ at Lascar summit (Tassi et al., 2009) and magma–derived water with $\delta^{18}O$ between +6 and +12‰ (Giggenbach et al., 1992; Taran et al., 1989). Part of the $^{18}O/^{16}O$ variations can also result

from equilibrium isotopic fractionation between the different sulphate minerals that are finely distributed within the crust.

Two observations suggest that the crust started to grow ca. 19 years before being sampled in 2012: (1) The fracture hosting the crust opened following the 1993 eruption (Matthews et al., 1997). (2) Lead and Sr isotope compositions indicate that the crust is genetically linked to the 1993 eruption, either through degassing of un-erupted magmas, or acid alteration of the rock on which the crust grew. The 2-3 mm thickness of the crust then requires an average growth rate of 0.3 - 0.4 μm/day. By comparison, the growth rates of sulphates formed in 850°C experiments are between less than 1μm/day for natural basalts and 2-7μm/day for glass (Johnson and Burnett, 1993).

6.2. Selective uptake of Tl, Te and V

The concentrations of Tl and Te are very elevated in the sulphate crust, but they are not unusual for fumarole deposits that commonly host Tl and Te gas sublimates. For instance, Tl and Te concentrations in excess of 2000 and 70 ppm, respectively, have been reported for Merapi (Indonesia), El Misti (Peru) and Vulcano (Italy) fumarole deposits (Kavalieris, 1994; Birnie and Hall, 1974; Fulignati and Sbrana, 1998). However, Tl and Te generally condense together with other metals of comparable volatility, such as Pb, Bi, Cd, Cu or Zn, which is not the case for the Lascar crust. Consequently ratios such as Tl/Pb (125-4558) and Te/Pb (28-2023) are orders of magnitude higher in the Lascar crust than in worldwide fumarolic gases, condensates and solid deposits, where they rarely exceed 3 and 10, respectively (Fig. 9). Only condensates from the fumaroles of the Avacha volcano (Kamchatka Peninsula, Russia), which are abnormally enriched in Tl (Okrugin et al., 2017), have Tl/Pb (up to 73) and Te/Pb (up to 36) ratios close to the Lascar crust values. On the other hand, Tl and Te concentrate in the crust together with V, which generally behaves as a non-volatile element in volcanic gases (Symonds et al., 1987; Mather et al., 2012), except in highly oxidizing conditions (Hughes and Stoiber, 1985; Taran et al., 2001).

Generally, the trace element chemistry of the crust appears unrelated to the chemistry of Lascar gases, which are enriched in As, Se, Bi, B, Zn, Pb, Sn, Mo, In, in addition to Te and Tl, and depleted in V and other refractory lithophile elements (Menard et al., 2014). This strongly suggests that the Tl, Te and V enrichments in the crust are not inherited from

the gas phase —in the sense that similar Tl-Te-V enrichments relative to other metals do not occur in gases—, but result from crust formation process. Both the gas phase and the host rock can supply Tl, Te and V to the crust. Although a dominant contribution from the gas phase is expected given the extreme enrichment of these elements in the crust, especially regarding Te that occurs at the ppb level in rocks, a contribution from rock cannot be ruled out. This possibility is taken into account in the calculation of the distribution coefficient of elements between crust and vapours ($D_{Crust/Gas}$):

$$D_{Crust/Gas} = [X]_{Cc}/[X]_{Gas} \quad (5)$$

with $[X]_{Cc} = [X]_C - [Zr]_C \,.\, [X]_R/[Zr]_R$

and $[X]_{Gas} = \{X\}_{Gas}/\{SO_2\}_{Gas} \,.\, [SO_2]_{Gas}$

where $[X]_{Cc}$ is the element concentration in the crust corrected for inputs from the rock, assuming all Zr originate from the altered rock. Zirconium is used because high-field strength elements are generally strongly depleted in magmatic gases. $[X]_C$ and $[X]_R$ are the measured concentrations in the crust outer layer (U1) and in 1993 lavas (Menard et al., 2014), respectively. $[X]_{Gas}$ is the mass fraction of elements in gases. $\{X\}_{Gas}$ and $\{SO_2\}_{Gas}$ are the volume-normalized masses of trace metal and SO_2 in the gas escaping from the fracture hosting the crust, respectively (sample Las 18 from Menard et al., 2014) (Fig 2a). $[SO_2]_{Gas}$ is the mass fraction of SO_2 estimated at 10% based on the composition of gases emanating from the active crater fractures with similar temperatures (285-385°C) (Tassi et al., 2009). The mass fraction of element originating from the gas phase ($[X]_{Cc}/[X]_C$) is estimated at < 30% for U and Hf, 50% for Pb and Rb, 66-82% for Co, Cu, Ni, Cr, Nb and Cs, 90-98% for Li, Zn, Bi, Cd and Sb, and >99% for As, Se, V, Mo, Tl, Te and S. $[X]_{Cc}/[X]_C$ is plotted against $D_{Crust/Gas}$ on Figure 10 for elements with $[X]_{Cc} > 0$. The generally high to very high values of $D_{Crust/Gas}$ reflect the very low content of trace metals in gases, in the range of 10^{-2} -10^{1} ppb. $D_{Crust/Gas}$ is ca. 4 for S, in the range of 1 – 5×10^{3} for Se, As and Sb, 10^{4} – 10^{5} for Pb, U, Zn, Hf, Cu, Rb, and 1–4×10^{5} for Cs, Mo, Cr, Ni, Co, Cd, Li and Nb. Tellurium, vanadium and thallium stand out, with $D_{Crust/Gas}$ between 6×10^{6} and 3.3×10^{7}. This order clearly does not reflect the volatility sequence of elements, but the ability of elements to enter the surface of the crust. For most elements $D_{Crust/Gas}$ does not

markedly change if the inner layer (U11) composition is used in the calculation. However, for Tl, V and Te $D_{Crust/Gas}$ decreases proportionally to the rim/core ratio (>20), and remains distinctly elevated only for Tl (1×10^6).

The enrichment of Tl and Te in the crust relative to the gas is comparable to that existing between Fe-Mn crust and seawater, in the range of 10^7 – 5×10^8 (Hein et al., 2003). The enrichment of V is higher in the fumarole crust than in seawater Fe-Mn crust (2×10^5). The enrichment of Tl, Te and other metals in marine Fe-Mn crust has been ascribed to oxidative sorption on, or structural incorporation in Mn oxides and Fe oxy-hydroxide (Hein et al., 2003, Peacock and Moon, 2012; Kashiwabara et al., 2014). Unlike marine crusts that concentrate 30+ elements by 6 orders of magnitude or more, the enrichment of Tl, Te and V in the fumarole crust is very selective and requires a very specific enrichment process.

6.3. Isomorphic substitution of Tl and V

Within the crust, Tl and V bearing phases are not detected at the highest resolution of scanning electron microscopy, indicating that Tl and V are in solid solution in the sulphate, or occur in the form of nanoparticles. The former possibility is strongly supported by the layered structure of alums that facilitates element substitution. Anhydrous alums are a series of more than 30 double sulphates sharing the general formula (Giester, 1994; West et al., 2008; Kosek et al., 2018):

$$M^{I}\,M^{III}\,(X^{VI}O_4)_2$$

where M^{I} is an univalent species (K^+, Na^+, Rb^+, Cs^+, Ag^+, Tl^+, NH_4^+), M^{III} is a trivalent metal (Al^{3+}, Fe^{3+}, Cr^{3+}, V^{3+}, Sc^{3+}, Mn^{3+}, Ga^{3+}, Rh^{3+}, In^{3+}, Tl^{3+}), X^{VI} is an hexavalent element (S^{6+}, Se^{6+}, Cr^{6+}, Mo^{6+}, W^{6+}). The structure of anhydrous alums consists of parallel sheets of $M^{III}O_6$ octahedra and $X^{VI}O_4$ tetrahedra, separated by large 12-fold coordinated M^{I} ions (West et al., 2008; Murashko et a., 2013; Zhitova et a.l., 2019). Isomorphic substitutions play an important role in alum composition and can be predicted from the ionic radii of elements (Shannon, 1976). Previous studies showed that univalent Tl (r=1.70Å) and trivalent V (r=0.64Å) tend to substitute for K^+ (r=1.64Å) and Al^{3+} (r=0.535 Å) respectively (see synthesis by Giester, 1994). In godovikovite, Tl^+ might substitute for

NH_4^+ (r=1.67Å for 12-fold coordination) (Sidey, 2016). The Tl-rich sulphate crystal lying on crust surface (Supplementary material S4) provides evidence for Tl incorporation into the crystal structure of alum. At magmatic temperature and oxygen fugacity, Tl and V dominantly occur in the gas phase as +1 (TlCl or Tl_2Cl_2) and +3 ions (VF_3 or VOCl), respectively (Hughes and Stoiber, 1985; Churakov et al., 2000). The enrichment of Tl and V in the Lascar crust is thus consistent with incorporation of gas derived Tl^+ and V^{3+} in the M^I and M^{III} sites, respectively, without change in valence state. Coupled incorporation of Tl and V might be energetically favourable since $TlV(SO_4)_2$ is a stable compound (Perret et al., 1972). This may result from Tl^+ and V^{3+} being both slightly larger than the ions they replace, limiting the distortion of the crystal network that may arise from individual substitution. Trivalent Tl, although generally of minor occurrence, can also probably significantly enter the M^{III} site as it does in potassium jarosite (Dutrizac et al., 2005).

6.4 Structural incorporation versus adsorption of Te

Unlike Tl and V, tellurium is not reported to enter the crystal structure of anhydrous alum, alum or alunite. This reflects the fact that Te^+ and Te^{3+} are unstable and Te^{6+} (0.43 Å), unlike Se^{6+}, is too large to substitute for four-fold coordinated S^{6+}(0.12 Å) in SO_4^{2-} (Shannon, 1976). Moreover, as discussed later for Mo (section 6.6.), Te concentration would not show a drastic increase towards crust rim if it were to substitute for sulphur. Tellurium is expected to be dominantly transported as $Te_{2(g)}$ (Grundler et al., 2013) in Lascar eccentric degassing system where redox conditions are governed by the Fe^{II}-Fe^{III} buffer of the rocks (Tassi et al. 2009, Giggenbach, 1987). Two processes of $Te_{2(g)}$ incorporation into the crust are envisioned. (a) The fact that Te correlates with Tl and V suggests that Te is incorporated by coupled substitution. For instance, $Te_{2(g)}$ could enter the M^I site via coupled substitution with trivalent Tl, in which two large Te^0 atoms (2.06 Å radius) and one small atom of Tl^{3+} (< 1 Å radius) substitute for three M^I atoms (ca. 1.7 Å radius). If this substitution controls the Te and Tl^{3+} budget of the crust, the atomic abundance of Te must be twice that of Tl^{3+}. The average measured (Tl^+ + Tl^{3+})/Te ratio of 2.2 then requires a somewhat realistic Tl^+/ Tl^{3+} atomic ratio of 3.3. (b) The occurrence of TeO_2 crystals on crust surface suggests that gaseous Te is adsorbed at the surface of anhydrous alum. Tellurium adsorption processes have been mainly described in

seawater and soils, where Te^{IV} and Te^{VI} species adsorb at the surface of $Fe^{(III)}$ hydroxides and illite via the formation of inner-sphere complexes (Hein et al., 2003, Kashiwabara et al., 2014; Qin et al., 2017). Adsorption of gaseous Te at the surface of mordenite zeolite has also been reported (Kodaira and Ikeda, 2014). This reaction occurs via sorption of nano- chains of Te atoms on dipoles formed by AlO_2^- and Na^+ in mordenite crystalline structure. The layers of $Al(SO4)_2^-$ and cations in anhydrous alums could represent reactive sites allowing Te sorption as for mordenite, but the occurrence of Te^{IV} on crust surface requires that tellurium oxidizes in a second step. The scenarios (a) and (b) are certainly not incompatible, because the adsorption process is the precursor to the chemisorption reaction, during which elements are incorporated in the crustal structure of sulphate (King et al., 2018).

6.5. Growth rate control on Tl-V-Te zonation

The concentrations of Tl, V and Te increase by a factor >20 from the core to the outer edge of the sulphate crust. This trend correlates with a decrease of the thickness of the growth layers, pointing out a control of growth rate on Tl, V and Te content (Fig. 11). Such growth rate control on metal abundance has been described in marine Fe-Mn crusts (e.g., Hein et al., 2003) where metal-rich hydrogenic phases are diluted by metal-poor detrital phases. The growth rate of the sulphate crust is controlled by the slow diffusion of rock cations by comparison to gas species. Rock cation supply is critical for the outermost layer of the mature crust because rock cations have to diffuse over long distances in the sulphate but also in the thick rock layer already depleted in cations (Fig. 8c). A straightforward consequence of the low rate of cation supply to the outermost layer of the crust is to favour the substitution of gas derived Tl, V and Te in the crystal structure of alum. The extremely elevated Tl-Te-V concentrations at crust rim thus first result from the lack of cations with which they compete for the M^I and M^{III} sites of anhydrous alum. In addition, as discussed for Te, it is possible that elements are adsorbed to some degree at the surface of the crust.

6.6. The molybdenum issue

Molybdenum stands out from Tl, V and Te because its elevated concentration in the crust (205-924 ppm) reflects a high concentration in the gas (32 ng/m^3) (Menard et al., 2014), and not an anomalously high crust/gas ratio (Fig. 10). The high Mo concentration of the gas might be related to its enrichment in HCl, which promotes Mo volatility in the form of MoO_2Cl_2 (Rempel et al., 2008). In addition, Mo does not show a comparable zonation as Tl-V-Te across the crust, but tends to correlate with S. This highlights a fundamental difference in the process by which Tl-Te-V and Mo are incorporated into the crust. In the absence of Mo mineral, Mo must also enter the crystal network of anhydrous alum. Unlike Te, Mo possibly enters the X^{VI} site (Giester, 1994) although Mo^{6+} (r=0.41 Å) is barely smaller than Te^{6+} (r=0.43 Å) in tetrahedral coordination (Shannon, 1976). Molybdenum essentially competes with S for this site. Because both Mo and S entirely originate from the gas phase (Fig. 10), the Mo content of the crust first depends on the Mo/S ratio of the gas, which has seemingly little varied during crust formation history (Mo/S=27±12×10^{-4}). Thus, the major difference between Tl-V-Te and Mo is that the formers compete with rock-derived cations, whose rate of supply decreases towards crust rim, whereas the second competes with another element of the gas.

6.7. Implications for trace element degassing

Figure 9 shows that the aerosols collected within the Lascar plume have four orders of magnitude lower Tl/Pb and Te/Pb compared to the fumarole crust, but remarkably similar Tl/Te ratio (1.5±0.6 (2σ) versus 3.6±2.7(2σ)). Likewise, aerosols and crust also have similar Tl/V ratio (0.54±0.42 (2σ) and 1.4±1.1(2σ), respectively). At Lascar, the small fractionation between Tl, Te and V contrasts with the large fractionation existing between Tl-Te-V and other volatile elements. This supports the idea that the underground partitioning of Tl, Te and V into anhydrous alums, such as godovikovite, significantly influences the abundance of these three elements in the gas plume. In the following, we evaluate quantitatively the effect of preferential incorporation of Tl over Pb into anhydrous alums on the Tl/Pb ratio. The trace element content of a gas equilibrating with a rock follows the general law of fluid/rock interaction:

$$[X]_G^f = \frac{[X]_R^i + N[X]_G^i}{N + D_{S/G}^X} \quad (6)$$

where $[X]_G^f$ and $[X]_G^i$ are the initial and final concentrations of element X in gas, $[X]_R^i$ is the initial concentration of X in rock, $D_{S/G}^X$ is the partition coefficient between solid and gas, and N is the gas/rock mass ratio. In the case of extensive gas-rock interaction, $[X]_R^i \ll N[X]_G^i$, and thus:

$$\left[\frac{Tl}{Pb}\right]_G^f = \frac{N+D_{S/G}^{Pb}}{N+D_{S/G}^{Tl}} \times \left[\frac{Tl}{Pb}\right]_G^i \quad (7)$$

Using distribution coefficients between crust surface and gas ($D_{S/G}^{Tl}=3.3\times10^7$ and $D_{S/G}^{Pb}=1.1\times10^4$) calculated as described in section 6.2, a gas/rock mass ratio between 1.6×10^6 and 1.0×10^7 is needed to decrease Tl/Pb from 1-5 in the initial gas (Johnson and Canil, 2011) to 0.23 in average Lascar aerosols (Menard et al., 2014). The sulphate crust formed by the interaction between gas and rock uptakes between 77 and 95% of the initial Tl content of the gases, but less than 1% of Pb. The fraction of Tl trapped in the ground translates into a daily deposition rate between 17 and 104 g, based on Lascar average Tl emission rate of 5 g/day (recalculated from Tl/SO_2 mass ratio of 10^{-8} in the gas plume and mean SO_2 flux of 500t/day from Menard et al. (2014) who erroneously calculated metal emission rates). The estimated fraction of Tl trapped underground should be considered as an upper bound, because it is likely that gases do not fully equilibrate with sulphates, and anhydrous alums might not form everywhere in the degassing network. For instance, 3 out of the 11 fumaroles sampled by Tassi et al. (2009) within Lascar active crater have temperature within the stability field of godovikovite.

Godovikovite has been discovered in burning coal-dumps in 1988, thus after the main surveys of fumarolic incrustations (Stoiber and Rose, 1974; Naughton et al., 1976; Oskarsson, 1981). This raises the possibility that godovikovite is more frequent than described in early reports. In support of this idea, godovikovite and isostructural steklite have been recently found in the fumarolic fields of Tolbachik, Mutnovsky and Avachinsky volcanoes, Kamchatka (Murashko et al., 2013 and M. Zelenski, personal communication). Generally, trapping of Tl in the ground is probably a widespread phenomenon due to the frequent occurrence of K-Na sulphates. For instance, Okrugin et al. (2017) noted that the altered rocks of Vulcano contain more than three orders of

magnitude more Tl (up to 280 ppm) than the fumarolic fluids (14–82 ppb Tl) (Cheynet et al. 2000; Boyce et al. 2007; Fulignati and Sbrana 1998). We hypothesize that Tl might substitute for K in alunite and for Na in natroalunite, which are common alteration phases at Vulcano (Boyce et al. 2007). Selective uptake of gaseous elements by isomorphic substitution in fumarolic minerals is not limited to Tl, Te and V. At Kilauea volcano, K and Cu might substitute for Na into thenardite (Naughton et al., 1976). At Mount St. Augustine, Alaska, Cr and V might substitute for Fe in fumarole incrustations (Kodosky and Keskinen; 1990). In high-sulphidation epithermal deposits, Ag^{+}-As^{3+}, and possibly Au^{3+}-Cu^{+} ion pairs substitute for Fe^{2+} into pyrite (Chouinard et al., 2005; Scher et al., 2013).

Selective entrapment of some gaseous elements into alteration minerals has significant consequences: (1) As modelled above, they can modify extensively key trace element ratios, such as Tl/Pb. At global scale, the Tl/Pb ratio of volcanic aerosols shows two order of magnitude variations (0.03 to 3.3), with no systematic difference between arc and hotspots volcanoes (Baker et al., 2009; Edmonds et al., 2018). Our results on the Lascar volcano suggest that Tl entrapment in alteration sulphates might explain part of the Tl/Pb variations in volcanic emanations, in addition to gas source heterogeneity (Okrugin et al., 2017), diffusive fractionation of Pb and Tl at the melt-gas interface (Johnson and Canil, 2011), and chemical evolution of gas during cooling (Churakov et al., 2000). (2) Substitution reactions potentially deplete volcanic emanations in some elements, which lead to underestimate the volatility of these latter. For instance V is the second most depleted element in the Lascar plume (Menard et al., 2014) although there is evidence from the studied crust that V is significantly transported by subsurface gases. (3) Highly toxic elements such as Tl are immobilized within volcanic edifices instead of being released in the atmosphere, in the same manner as heavy metals are retained by alunite group minerals in polluted sites (Kolitsch and Pring, 2001; Figueiredo and da Silva, 2011). Thallium pollution of soils around Lascar volcano is an example of such local impact (Queirolo et al., 2009).

7) Conclusions

This study of the fine-scale chemical and isotopic zonation of an underground fumarolic crust from the Lascar volcano reached the following conclusions:

(1) Magmatic-hydrothermal gases from the Lascar volcano, 330°C in temperature, precipitate anhydrous alums underground as they react with rocks. The studied specimen occurs as a few millimetres thick crust that grew internally by poly-diffusion reactions within the sulphate. The growth rate is on average 0.3 μm/day, but decreases towards crust rim due to the slow diffusive influx of rock cations.

(2) The crust selectively uptakes gaseous Tl, V and Te and, to a lesser extent Mo. This uptake results from the incorporation of the elements into the crystal structure of alum: Tl^{+}, V^{3+} and Mo^{6+} substitute for K^{+}, Al^{3+} and S^{6+} into the M^{I}, M^{III} and X^{VI} sites of alum, respectively. The process of Te uptake remains uncertain, but must be tightly related to Tl-V incorporation.

(3) The extent of Tl, V and Te uptake is the highest at the outer edge of the crust, where the low rate of rock cations supply favours the substitution process. Such surface enrichment does not occur for Mo, because Mo competes with S, which is continuously supplied from the gas. Thus, the extreme enrichment of Tl, V and Te at the surface of the mature alum crust first reflects their ability to substitute for rock-derived cations and to compensate for their lack.

(4) Gases equilibrating with anhydrous alums lose a large amount of Tl, V and Te, but insignificant amount of other volatile trace elements (Pb, Cu, Zn, Bi, Sb, As, Se). This dramatically fractionates key trace elements ratios in volcanic emanations, such as Pb/Tl, or Se/Te. This also decreases the amount of Tl, V and Te released in the atmosphere. Immobilization of toxic Tl within the Lascar volcano contributes to the local Tl soil-pollution.

(5) Sub-surface gas-rock interaction within stratovolcanoes acts as a filter stripping some elements from the gas phase. A better understanding of the mechanism and extent of incorporation of metals and metalloids in the wide range of fumarole alteration minerals is needed to evaluate quantitatively the impact of underground gas-rock interaction on the degassing fluxes of volcanoes.

Supplementary material

Table S1 : In situ major and trace element concentrations

Table S2 : In situ oxygen isotope composition

Table S3 : Bulk Pb and Sr isotope compositions

Supplementary material S4: Electron microscopy survey of crust surface

Acknowledgements

J.L. Devidal, J.M. Henot, N. Bouden, C. Fonquernie, D. Auclair and A. Gannoun contributed to data acquisition. We thank M. Zelenski and two anonymous reviewers for their constructive comments, and G. Pokrovski for handling the manuscript. This work benefited from the financial support from the Institut de Recherche pour le Développement (ECOS-sud project no. C11U01, P.I. O. Roche), the French Government Laboratory of Excellence initiative n°ANR-10-LABX-0006, the Région Auvergne and the European Regional Development Funds. This is Laboratory of Excellence ClerVolc contribution number XXX.

Figure captions

Figure 1

Location maps. (a) Schematic map of northern Chile showing the location of the Lascar volcano. (b) Schematic map of Lascar craters showing the degassing fracture (star) where the fumarolic crust was sampled in November 2012 (modified from Menard et al., 2014).

Figure 2

Sampling site and crust sample. (a) Thermal image showing the location of gas sampling (filter packs) ca. 2m from the degassing hole. (b) Thermal image of the degassing hole where the crust was sampled in November 2012. (c) Photo of the degassing hole. Arrow indicates the lava block under which the crust was sampled. (d) Drawing of the crust and the host rock, respecting size proportions. (e) Photo of crust surface showing several outgrowths, more or less cracked and hollow. (f) Polished section of the studied outgrowth showing growth layers and the area selected for in-situ chemical analyses.

Figure 3

Raman spectra of the three major phases. (a) 100-1300 cm^{-1} range. (b) 2900-3700 cm^{-1} range. Characteristic vibration bands of $(NH_4)Al(SO_4)_2$ (godovikovite), $MgSO_4{\cdot}6H_2O$ (exahydrite), $CaSO_4$ (anhydrite) and hydrated alums (990/991 cm^{-1}) are indicated.

Figure 4

SEM image of the studied crust section. (a) Concentric growth layers and spot locations of EPMA and ICPMS analyses are highlighted. (b-d) Mapping of Al, Fe and Ca.

Figure 5

Lava-normalized trace element concentrations. Normalized concentrations are shown for crust core (average of unit 11) and crust rim (average of unit 1). Because Se was not measured by LA-ICPMS, the bulk Se concentration in crust surface scrapings (2.4±1.2 ppm) is used. Concentrations of the 1993 lava used for normalization are from Menard et al. (2014). Elements are sorted from left to right according to their increasing

enrichment in crust core. Propagated error on lava-normalized trace element concentrations is within symbol size.

Figure 6

Chemical variations across the crust. (a) Thallium, vanadium and tellurium concentrations plotted against distance to crust rim. Data are from profile A1. Profile A2 (not plotted) shows the same variations. Error on trace element concentrations is within symbol size. (b) Tl/V, Tl/Te and V/Te concentration ratios plotted against distance to crust rim.

Figure 7

Core-rim $\delta^{18}O$ profiles. The three profiles (B1, B2 and B3) are normalized to the length of the A1 profile. The average in-run error (0.25‰, 2σ) is indicated. The grey band indicates the $\delta^{18}O$ of Lascar fumaroles condensates (Tassi et al., 2009). Compositions of local meteoric water (Tassi et al., 2009) and andesitic water (Giggenbach, 1992; Taran et al., 1989) are indicated.

Figure 8

Schematic drawing of the processes leading to the formation of a thick alum crust. (a) A sulphate layer grows via diffusive influx of rock cations and two-way diffusion of reaction gases within the sulphate. Gaseous NH_3 and trace metals (Tl, V and Te) are incorporated into the crust following Eqs. 2-4. (b) Internal sulphate growth results in stress accumulation within the coating (σ). The thickening sulphate layer detaches from the rock surface, wrinkles and buckles. The layer also starts to split into two layers due to higher growth rate near the sulphate-rock interface. (c) As the sulphate crust grows, the exhaustion of cations in the reacted rock requires cations to migrate over longer distances. The growth rate decreases towards crust surface due to the low rate of rock cations supply. This results in the formation of thinner growth layers at the outer edge of the crust. The lack of rock cations also favours the substitution of Tl, V and probably Te into the crystal structure of alum, yielding the extreme enrichment observed at crust rim. (a-c) Grey scale indicates the depletion of major cations in the silicate, white colour corresponding to SiO_2. (a) and (b) are modified from Renggli et al., (2018).

Figure 9

Te/Pb versus Tl/Pb plot comparing the signature of Lascar crust and aerosols to those of worldwide volcanic aerosols, fumarole condensates and solid deposits. Propagated error on trace element ratios is within symbol size (Lascar data). Lascar aerosol data are from Menard et al. (2014). Other data are from Kavalieris (1994), Moune et al. (2010), Zelenski et al. (2013, 2014), Chaplygin et al. (2016), Taran et al. (1995), Zelenski and Bortnikova (2005), Okrugin et al. (2017), Fulignati and Sbrana (1998), Boyce et al. (2007), Gauthier et al. (2016) and Mather et al. (2012).

Figure 10

Crust/gas distribution coefficient plotted against element fraction originating from the gas. Distribution coefficients are calculated by normalizing the concentration of elements in the outer shell of the Lascar crust (U1 layer) to their abundance in the gas escaping from the fracture hosting the crust. Crust concentrations are corrected for rock inputs, as explained in text.

Figure 11

Correlation between 1/Tl and growth layer thickness, a proxy for crust growth rate. Median values are plotted for each unit. Error bars on x and y axis indicate upper and lower bounds for each layer.

References

Africano F. and Bernard A. (2000) Acidic alteration in the fumarolic environment of Usu volcano, Hokkaido, Japan. *J. Volcanol. Geotherm. Res.* **97**, 475-495.

Allard P., Aiuppa A., Loyer H., Carrot F., Gaudry A., Pinte G., Michel A. and Dongarrà G. (2000) Acid gas and metal emission rates during long lived basalt degassing at Stromboli volcano. *Geophys. Res. Lett.* **27**, 1207–1210.

Baker R.G.A., Rehkämper M., Hinkley T.K., Nielsen S.G. and Toutain, J.-P. (2009) Investigation of thallium fluxes from subaerial volcanism—Implication for the present and past mass balance of thallium in the oceans. *Geochim. Cosmochim. Acta* **73**, 6340-6359.

Balic Zunic T., Moëlo Y., Loncar Z. and Micheelsen H. (1994) Dorallcharite, $Tl_{0.8}K_{0.2}Fe_3(SO_4)_2(OH)_6$, a new member of the jarosite-alunite family. *Eur. J. Mineral.* **6**, 255-263

Bernard A. and Le Guern F. (1986) Condensation of volatile elements in high-temperature gases of Mount St. Helens. *J. Volcanol. Geotherm. Res.* **28**, 91-105.

Birnie R.W. and Hall J.H. (1974) The geochemistry of El Misti volcano, Peru fumaroles. *Bull. Volcanol.* **38**, 1.

Boyce A.J., Fulignati P., Sbrana A. and Fallick A.E. (2007) Fluids in early stage hydrothermal alteration of high-sulfidation epithermal systems: A view from the Vulcano active hydrothermal system (Aeolian Island, Italy). *J. Volcanol. Geotherm. Res.* **166**, 76–90.

Bunsen R. (1851) Ueber die Processe der vulkanischen Gesteinsbildungen Islands. *Ann Phys* **159**, 197–272.

Chaplygin I.V., Lavrushin V.Y., Dubinina E.O., Bychkova Y.V., Inguaggiato S. and Yudovskaya M.A. (2016) Geochemistry of volcanic gas at the 2012–13 New Tolbachik eruption, Kamchatka. *J. Volcanol. Geotherm. Res.* **323**, 186-193.

Cheynet B., Dall'Aglio M., Garavelli A., Grasso M.F. and Vurro F. (2000) Trace elements from fumaroles at Vulcano Island (Italy): Rates of transport and a thermochemical model. *J. Volcanol. Geotherm. Res.* **95**, 273–283.

Chouinard A., Paquette J. and Williams-Jones A.E. (2005) Crystallographic controls on trace-element incorporation in auriferous pyrite from the Pascua epithermal high-sulfidation deposit, Chile-Argentina. *Can. Mineral.* **43**, 951–963.

Churakov S.V., Tkachenko S.I., Korzhinskii M.A., Bocharnikov R.E. and Shmulovich K.I., (2000). Evolution of composition of high-temperature fumarolic gases from Kudryavy Volcano, Iturup, Kuril Islands: the thermodynamic modeling. *Geochem. Int.* **38**, 436–451.

Doukas M.P. and T.M. Gerlach (1995) Sulfur Dioxide Scrubbing During the 1992 Eruptions of Crater Peak, Mount Spurr Volcano, Alaska. In: Keith, T.E.C. (Ed.), The 1992 Eruptions of Crater Peak Vent, Mount Spurr Volcano, Alaska. *U.S. Geol. Surv. Bull.* **2139**, 47-57.

Dutrizac J.E. and Jambor J.L. (2000) Jarosites and their application in hydrometallurgy. *Rev. Mineral. Geochem.* **40**, 405–452.

Dutrizac J.E., Chen T.T. and Beauchemin S. (2005) The behaviour of thallium(III) during jarosite precipitation. *Hydrometallurgy* **79**, 138– 153.

Edmonds M., Mather T.A. and Liu E.J. (2018) A distinct metal fingerprint in arc volcanic emissions. *Nat. Geosci.* **11**, 790–794.

Ericksen G. (1983). The Chilean nitrate deposits. *Am. Scientist* **71**, 366-374.

Figueiredo M.-O. and da Silva T.P. (2011) The Positive environmental contribution of jarosite by retaining lead in acid mine drainage areas. *Int. J. Environ. Res. Public Health* **8**, 1575-1582.

Frezzotti M.L., Tecce F. and Casagli A. (2012) Raman spectroscopy for fluid inclusion analysis. *J. Geochem. Expl.* **112**, 1-20.

Fulignati P. and Sbrana A. (1998) Presence of native gold and tellurium in the active high-sulfidation hydrothermal system of the La Fossa volcano (Vulcano Italy). *J. Volcanol. Geotherm. Res.* **86**, 187–198.

Gardeweg M.C., Sparks R.S.J. and Matthews S.J. (1998) Evolution of Lascar Volcano. *J. Geol. Soc. Lond.* **155**, 89–104.

Gardeweg M., Amigo A., Matthews S., Sparks S. and Clavero, J. (2011) Geología del volcán Lascar, Región de Antofagasta. Carta Geológica de Chile No 131, Servicio. Nac. Geol. Min, 40 p.

Gauthier P.-J., Sigmarsson O, Gouhier M., Haddadi B. and Moune S. (2016) Elevated gas flux and trace metal degassing from the 2014–2015 fissure eruption at the Bárðarbunga volcanic system, Iceland. *J. Geophys. Res. (Solid Earth)* **121**, 1610–1630.

Getahun A., Reed M.H. and Symonds R. (1996) Mount St. Augustine volcano fumarole wall rock alteration: mineralogy, zoning, composition and numerical models of its formation process. *J. Volcanol. Geotherm. Res.* **71**, 73-107.

Giggenbach W.F. (1992) Isotopic shifts in waters from geothermal and volcanic systems along convergent plate boundaries and their origin. *Earth Planet Sci Lett* **113**, 495–510.

Giester G. (1994) Crystal structure of anhydrous alum $RbFe^{3+}(SeO_4)_2$. *Monatsh. Chem.* **125**, 1223-1228.

Grundler P. V., Brugger J., Etschmann B. E., Helm L., Liu W., Spry P.G., Tian Y., Testemale D. and Pring A. (2013) Speciation of aqueous tellurium(IV) in hydrothermal solutions and vapors, and the role of oxidized tellurium species in Te transport and gold deposition. *Geochim. Cosmochim. Acta* **120**, 298–325.

Hein J. R., Koschinsky A. and Halliday A. N. (2003) Global occurrence of tellurium-rich ferromanganese crusts and a model for the enrichment of tellurium. *Geochim. Cosmochim. Acta* **67**, 1117–1127.

Henley R.W., Mavrogenes J. and Tanner D. (2012) Sulfosalt melts and heavy metal (As-Sb-Bi-Sn-Pb-Tl) fractionation during volcanic gas expansion: the El Indio (Chile) paleo-fumarole. *Geofluids* **12**, 199–215.

Henley R.W. and Berger B.R. (2013) Nature's refineries— Metals and metalloids in arc volcanoes. *Earth Sci. Rev.* **125**, 146–170.

Henley R.W., King P.L., Wykes J.L., Renggli C.J., Brink F.J., Clark D.A. and Troitzsch U. (2015) Porphyry copper deposit formation by sub-volcanic sulphur dioxide flux and chemisorption. *Nat. Geosci.* **8**, 210–215.

Henley R.W. and Seward T.M. (2018) Gas–solid reactions in arc volcanoes: Ancient and modern. *Rev. Mineral. Geochem.* **84**, 309-349.

Hughes J.M. and Stoiber R.E. (1985) Vanadium sublimates from the fumaroles of Izalco volcano, El Salvador. *J. Volcanol. Geotherm. Res.* **24**, 283-291.

Jochum K.P., Nohl U., Herwig K., Lammel E., Stoll B. and Hofmann A.W. (2005) GeoReM: A new geochemical database for reference materials and isotopic standards. *Geostand. Geoanal. Res.* **29**, 333-338.

Johnson M.L. and Burnett D.S. (1993) SO_2–rock interaction on Io: Reaction under highly oxidizing conditions. *J. Geophys. Res.* **98**, 1223–1230.

Johnson A. and Canil, D. (2011) The degassing behavior of Au, Tl, As, Pb, Re, Cd and Bi from silicate liquids: experiments and applications. *Geochim. Cosmochim. Acta* **75**, 1773–1784.

Kashiwabara T., Oishi Y., Sakaguchi A., Sugiyama T., Usui, A. and Takahashi Y. (2014) Chemical processes for the extreme enrichment of tellurium into marine ferromanganese oxides. *Geochim. Cosmochim. Acta* **131**, 150-163.

Kavalieris I. (1994) High Au, Ag, Mo, Pb, V and W content of fumarolic deposits at Merapi volcano, central Java, Indonesia. *J. Geochem. Explor.* **50**, 479-491.

King P.L., Wheeler V.M., Renggli C.J., Palm A.B., Wilson S.A., Harrison A.L., Morgan B., Nekvasil H., Troitzsch U., Mernagh T. et al. (2018) Gas–solid reactions: Theory, experiments and case studies relevant to earth and planetary processes. *Rev. Mineral. Geochem.* **84**, 1-56.

Kodaira T. and Ikedab T. (2014) The selective adsorption of tellurium in the aluminosilicate regions of AFI- and MOR-type microporous crystals. *Dalton Trans.* **43**, 13979-13987.

Kodosky L. and Keskinen M. (1990) Fumarole distribution, morphology, and encrustation mineralogy associated with the 1986 eruptive deposits of Mount St. Augustine, Alaska. *Bull. Volcanol.* **52**, 175-185.

Kolitsch U. and Pring A. (2001) Crystal chemistry of the crandallite, beudantite and alunite groups: a review and evaluation of the suitability as storage materials for toxic metals. *J. Min. Petrol. Sci.* **96**, 67-78.

Kosek F., Culka A. and Jehlicka, J. (2018) Raman spectroscopic study of six synthetic anhydrous sulfates relevant to the mineralogy of fumaroles. *J. Raman Spectrosc.* **49**, 1205-1216.

Le Guern F., Cheynet B. and Faivre-Pierret R.X. (1993) Characterization and modelling of the complete volcanic gas phase. *Geochem. J.* **27**, 323-336.

Lipson H., Beevers C.A. and Bragg W.L. (1935) The crystal structure of the alums. 148 Proc. Royal Soc. London. Series A – Math. Phys. Sci. https://doi.org/10.1098/rspa.1935.0040.

Lowenstern J.B., Janik C.J., Fournier R.O., Tesfai T., Duffield W.A., Clynne M.A., Smith J.G., Woldegiorgis L., Weldemariam K. and Kahsai G. (1999) A geochemical reconnaissance of the Alid volcanic center and geothermal system, Danakil depression, Eritrea. *Geothermics* **28**, 161-187.

Mather T. A., Witt M.L.I., Pyle D.M., Quayle B.M., Aiuppa A., Bagnato E., Martin R.S., Sims K.W.W., Edmonds M., Sutton A.J. et al. (2012), Halogens and trace metal emissions from the on-going 2008 summit eruption of Kīlauea volcano, Hawai'i. *Geochim. Cosmochim. Acta* **83**, 292–323.

Matthews S.J., Gardeweg M.C. and Sparks, R.S.J. (1997) The 1984 to 1996 cyclic activity of Lascar volcano, northern Chile: cycles of dome growth, dome subsidence, degassing and explosive eruptions. *Bull. Volcanol.* **59**, 72–82.

Matthews S.J., Sparks R.S.J. and Gardeweg, M.C. (1999) The Piedras Grandes-Soncor eruptions, Lascar Volcano, Chile; evolution of a zoned magma chamber in the Central Andean upper crust. *J. Petrol.* **40**, 1891–1919.

Menard G., Moune S., Vlastélic I., Aguilera F., Valade S. and Bontemps M. (2014) Gas and aerosol emissions from Lascar volcano (northern Chile): insights into the origin of gases and their links with the volcanic activity. *J. Volcanol. Geotherm. Res.* **287**, 51–67.

Mindat.org database (2019) Godovikovite: Mineral information, data and localities. https://www.mindat.org/min-1717.html.

Moune S., Gauthier P.-J. and Delmelle P. (2010) Trace elements in the particulate phase of the plume of Masaya Volcano, Nicaragua. . *J. Volcanol. Geotherm. Res.* **193**, 232-244.

Murashko M., Pekov I., Krivovichev S., Chernyatyeva A., Yapaskurt V., Zadov A. and Zelensky, M. (2013) Steklite, $KAl(SO_4)_2$: A finding at the Tolbachik Volcano, Kamchatka, Russia, validating its status as a mineral species and crystal structure. *Geol. Ore Deposits* **55**, 594-600.

Naughton J.J., Greenberg V.A. and Goguel R. (1976) Incrustations and fumarolic condensates at kilauea volcano, Hawaii: field, drill-hole and laboratory observations. *J. Volcanol. Geotherm. Res.* **1**, 149-165.

Okrugin V., Favero M., Liu A., Etschmann B., Plutachina E., Mills S., Tomkins A.G., Lukasheva M., Kozlov V., Moskaleva S. et al. (2017) Smoking gun for thallium geochemistry in volcanic arcs: Nataliyamalikite, TlI, a new thallium mineral from an active fumarole at Avacha Volcano, Kamchatka Peninsula, Russia. *Am. Mineral.* **102**, 1736-1746.

Oskarsson N. (1981) The chemistry of Icelandic lava incrustations and the latest stages of degassing. *J. Volcanol. Geotherm. Res.* **10**, 93–111.

Palm A.B., King P.L., Renggli C.J., Hervig R.L., Dalby K.N., Herring A., Mernagh T.P., Eggins S.M., Troitzsch U., Beeching L. et al. (2018) Unravelling the Consequences of SO2–Basalt Reactions for Geochemical Fractionation and Mineral Formation. *Mineral. Geochem.* **84**, 257-283.

Parafiniuk J. and Kruszewski L. (2009) Ammonium minerals from burning coal-dumps of the Upper Silesian Coal Basin (Poland). *Geol. Quarterly* **53**, 341-356.

Peacock C. and Moon E.M. (2012) Oxidative scavenging of thallium by birnessite: explanation for thallium enrichment and stable isotope fractionation in marine ferromanganese precipitates. *Geochim. Cosmochim. Acta* **84**, 297–313.

Perret R., Thrierr A. and Couchot P. (1972) Sur les « aluns anhydres » de vanadium. Préparation et étude cristallographique de $NH_4V(SO_4)_2$, $TlV(SO_4)_2$, $NaV(SO_4)_2$ et $AgV(SO_4)_2$. In: Bulletin de la Société française de Minéralogie et de Cristallographie, vol. 95, 4, 1972. pp. 521-524.

Pfister L., Thielen F., Deloule E., Valle N., Lentzen E., Grave C., Beisel J.-N. and McDonnell J.J., (2018) Freshwater pearl mussels as a stream water stable isotope recorder. *Ecohydrology* **11**, doi: 10.1002/eco.2007.

Qin H.-B., Takeichi Y., Nitani H., Terada Y. and Takahashi Y. (2017) Tellurium Distribution and Speciation in Contaminated Soils from Abandoned Mine Tailings: Comparison with Selenium. *Environ Sci Technol* **51**, 6027−6035.

Queirolo F., Stegen S., Contreras-Ortega C., Ostapczuk P., Queirolo A. and Paredes B. (2009) Thallium levels and bioaccumulation in environmental samples of Northern Chile: Human health risks. *J. Chil. Chem. Soc.* **54**, 464-469.

Rempel K.U., Williams-Jones A.E. and Migdisov A.A. (2008) The solubility of molybdenum dioxide and trioxide in HCl-bearing water vapour at 350°C and pressures up to 160 bars. *Geochim. Cosmochim. Acta* **72**, 3074–3083.

Renggli C.J. and King P.L. (2018) SO_2 Gas Reactions with Silicate Glasses. *Mineral. Geochem.* **84**, 229-255.

Risacher F. and Alonso H. (2001) Geochemistry of ash leachates from the 1993 Lascar eruption, northern Chile. Implication for recycling of ancient evaporates. *J. Volcanol. Geotherm. Res.* **109**, 319-337.

Rosner M., Erzinger J., Franz G. and Trumbull R.B. (2003) Slab-derived boron isotope signatures in arc volcanic rocks from the Central Andes and evidence for boron

isotope fractionation during progressive slab dehydration. *Geochem. Geophys. Geosyst.* **4**, doi:10.1029/2002GC000438.

Scher S., Williams-Jones A.E. and Williams-Jones G. (2013) Fumarolic Activity, Acid-Sulfate Alteration, and High Sulfidation Epithermal Precious Metal Mineralization in the Crater of Kawah Ijen Volcano, Java, Indonesia. *Econ. Geol.* **108**, 1099-1118.

Shannon, R. D. (1976) Revised effective ionic radii and systematic studies of interatomic distances in halides and chalcogenides. *Acta Cryst.* **A32**, 751–767.

Shimobayashi N., Ohnishi M. and Miura H. (2011) Ammonium sulfate minerals from Mikasa, Hokkaido, Japan: boussingaultite, godovikovite, efremovite and tschermigite. *J. Mineral. Petrol. Sci.* **106**, 158-163.

Sidey V. (2016) On the effective ionic radii for ammonium. *Acta Cryst.* **B72**, 626–633

Snyder G., Poreda R., Fehn U. and Hunt A. (2003) Sources of nitrogen and methane in Central American geothermal settings: Noble gas and ^{129}I evidence for crustal and magmatic volatile components, *Geochem. Geophys. Geosyst.* **4**, 9001, doi:10.1029/2002GC000363, 2003.

Stern C. (2004) Active Andean volcanism: its geologic and tectonic setting. *Rev. Geol. Chile* **31**, 161–206.

Stoiber R. E. and Rose W. I. (1974) Fumarole incrustations at active Central American volcanoes. *Geochim. Cosmochim. Acta* **38**, 495–516.

Symonds R.B., Rose W.I., Reed M.H., Lichte F.E. and Finnegan D.L. (1987) Volatilization, transport and sublimation of metallic and non-metallic elements in high temperature gases at Merapi Volcano, Indonesia. *Geochim. Cosmochim. Acta* **51**, 2083-2101.

Symonds R.B., Reed M.H. and Rose W.I. (1992) Origin, speciation, and fluxes of trace-element gases at Augustine volcano, Alaska: Insight into magma degassing and fumarolic processes. *Geochim. Cosmochim. Acta* **56**, 633-657.

Symonds R.B., Gerlach T.M. and Reed M.H. (2001) Magmatic gas scrubbing: implications for volcano monitoring. *J. Volcanol. Geotherm. Res.* **108**, 303-341.

Taran Y.A., Pokrovsky B.G. and Esikov A.D. (1989) Deuterium and oxygen-18 in fumarolic steam and amphiboles from some Kamchatka volcanoes: "andesitic waters". *Dokl. Akad. Nauk USSR* **304**, 440–443.

Taran Y.A., Hedenquist J.W., Korzhinsky M.A., Tkachenko S.I. and Shmulovich K.I. (1995) Geochemistry of magmatic gases from Kudryavy volcano, Iturup, Kuril Islands. *Geochim. Cosmochim. Acta* **59**, 1749-1761.

Taran Y.A., Bernard A., Gavilanes J.-C., Lunezheva E., Cortés A. and Armienta M.A. (2001) Chemistry and mineralogy of high-temperature gas discharges from Colima volcano, Mexico. Implications for magmatic gas–atmosphere interaction. *J. Volcanol. Geotherm. Res.* **108**, 245-264.

Tassi F., Aguilera F., Vaselli O., Medina E., Tedesco D., Delgado Huertas A., Poreda R. and Kojima S. (2009) The magmatic- and hydrothermal-dominated fumarolic system at the Active Crater of Lascar Volcano, northern Chile. *Bull. Volcanol.* **71**, 171–183.

Vlastélic I., Staudacher T., Deniel C., Devidal J.L., Devouard B., Finizola A. and Télouk P. (2013) Lead isotopes behavior in the fumarolic environment of the Piton de la Fournaise volcano (Réunion Island). *Geochim. Cosmochim. Acta* **100**, 297-314.

West D.V., Huang Q., Zandbergen H.W., McQueen T.M. and Cava R.J. (2008) Structural disorder, octahedral coordination and two-dimensional ferromagnetism in anhydrous alums. *J. Solid State Chem.* **181**, 2768-2775.

Zelenski M.E. and Bortnikova S. (2005) Sublimate speciation at Mutnovsky volcano, Kamchatka. *Eur. J. Mineral.* **17**, 107-118.

Zelenski M.E., Fischer T. P., de Moor J.M., Marty B., Zimmermann L., Ayalew D., Nekrasov A.N. and Karandashev V.K. (2013), Trace elements in the gas emissions from the Erta-Ale volcano, Afar, Ethiopia. *Chem. Geol.* **357**, 95–116.

Zelenski M.E., Malik N. and Taran Y. (2014) Emissions of trace elements during the 2012–2013 effusive eruption of Tolbachik volcano, Kamchatka: enrichment factors, partition coefficients and aerosol contribution. *J. Volcanol. Geotherm. Res.* **285**, 136-149.

Zhitova E.S., Sergeeva A.V., Nuzhdaev A.A., Krzhizhanovskaya M.G. and Chubarov V.M. (2019) Tschermigite from thermal fields of Southern Kamchatka: high-temperature transformation and peculiarities of IR-spectrum. *Proc. Russ. Mineral. Soc.* **148**, 110-116.

Zimbelman D.R., Rye R.O. and Breit G.N. (2005) Origin of secondary sulfate minerals on active andesitic stratovolcanoes. *Chem. Geol.* **215**, 37– 60.

Figure 1

F1

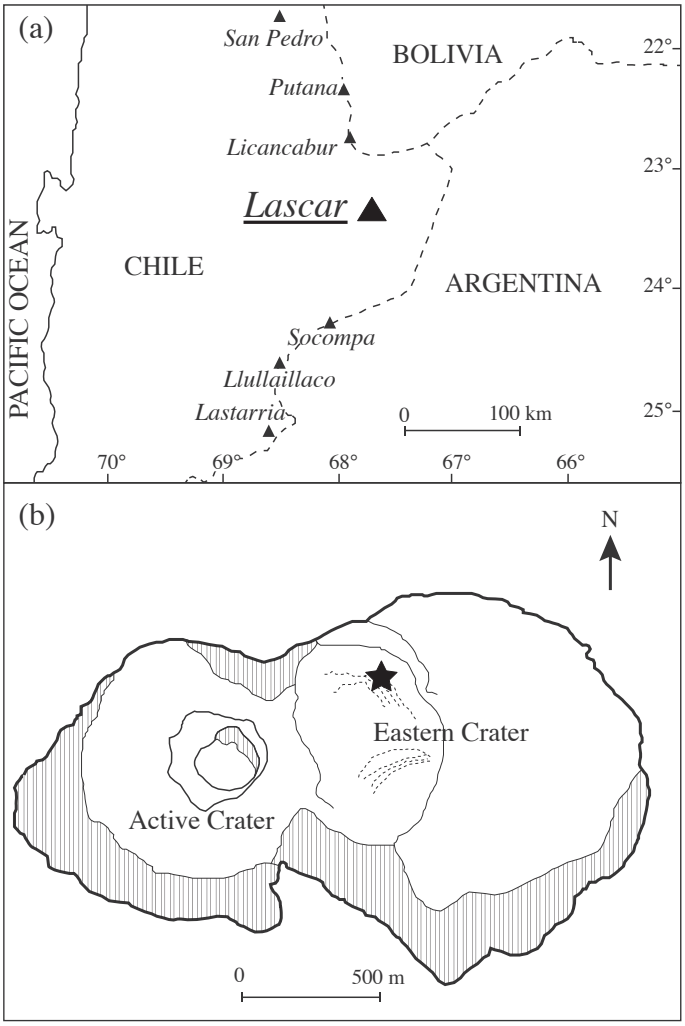
(a)
San Pedro
BOLIVIA
22°
Putana
Licancabur
23°
Lascar
PACIFIC OCEAN
CHILE
ARGENTINA
24°
Socompa
Llullaillaco
Lastarria
0
100 km
25°
70°
69°
68°
67°
66°
(b)
N
Eastern Crater
Active Crater
0
500 m

Figure 2

F2

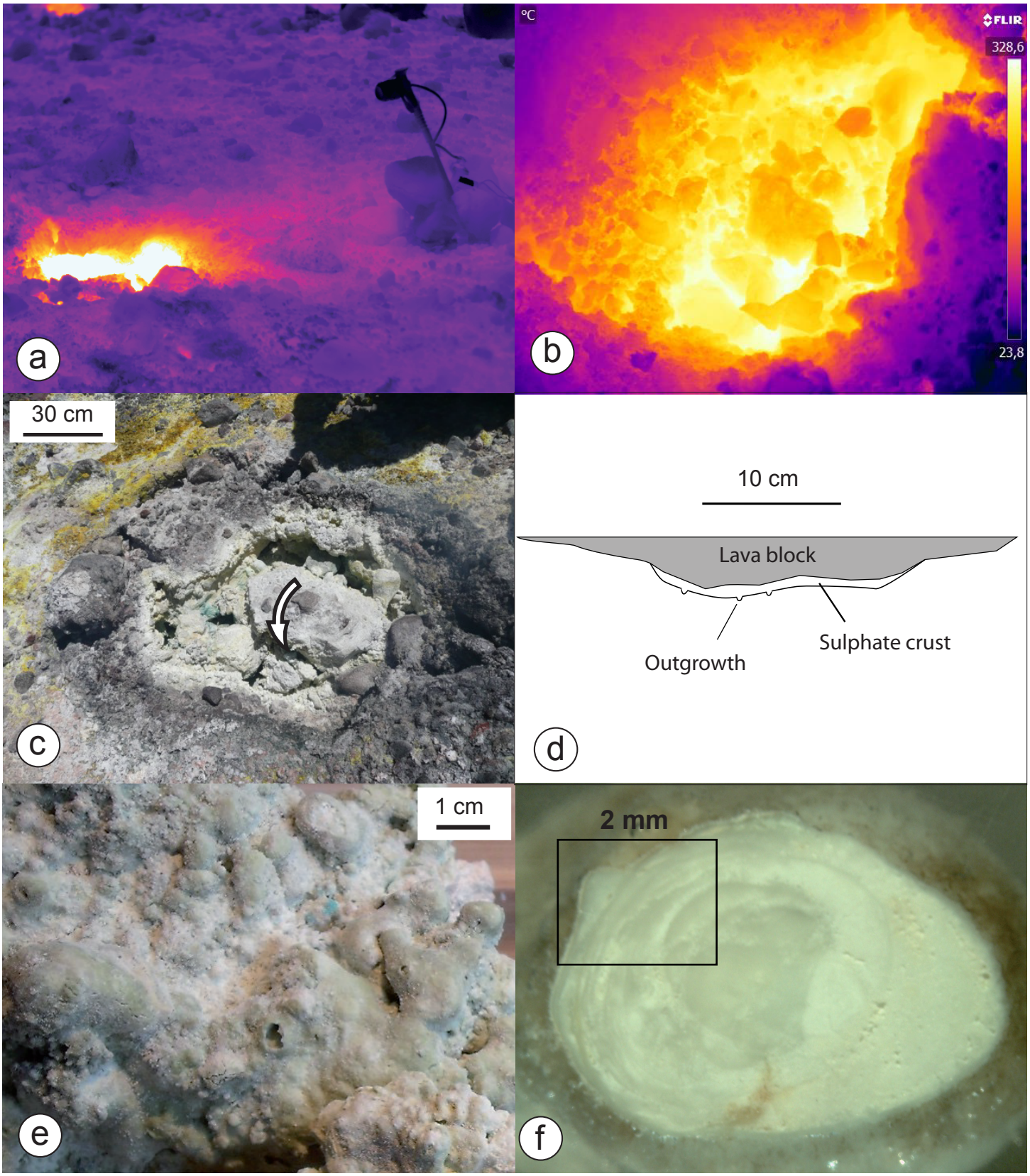
a
b
°C
FLIR
328,6
23,8
30 cm
c
10 cm
Lava block
Sulphate crust
Outgrowth
d
1 cm
e
2 mm
f

Figure 3

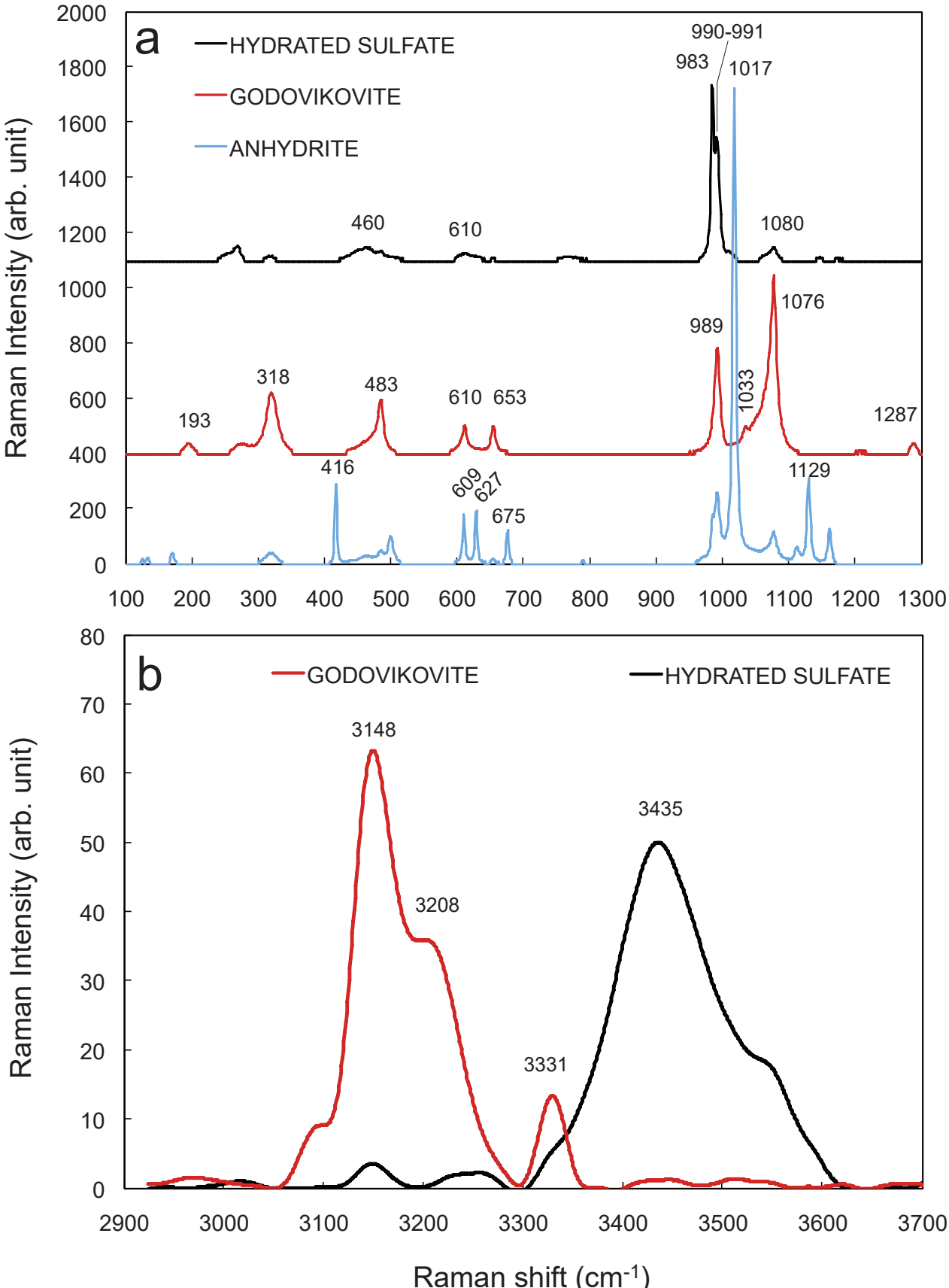
a
HYDRATED SULFATE
GODOVIKOVITE
ANHYDRITE
990-991
983
1017
460
610
1080
1076
989
318
483
610
653
1033
193
1287
416
1129
609
627
675
Raman Intensity (arb. unit)
b
GODOVIKOVITE
HYDRATED SULFATE
3148
3435
3208
3331
Raman Intensity (arb. unit)
Raman shift (cm-1)

Figure 4

F4

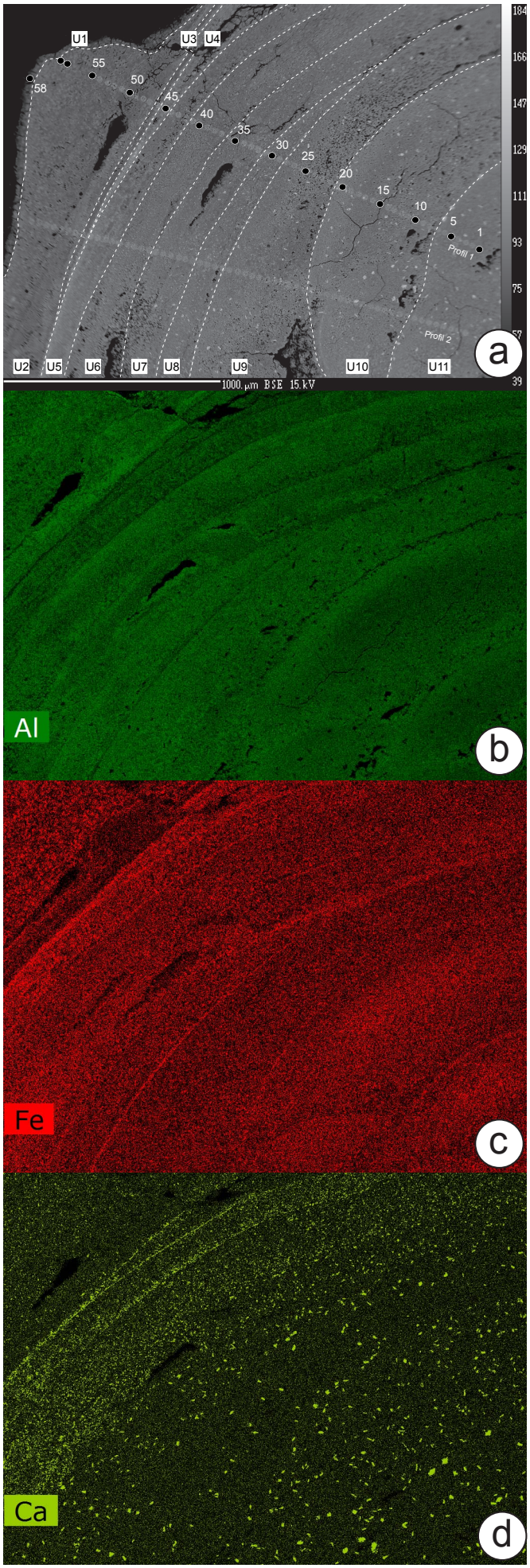
U1
U3
U4
55
58
50
45
40
35
30
25
20
15
10
5
1
Profil 1
Profil 2
U2
U5
U6
U7
U8
U9
U10
U11
1000 µm BSE 15 kV
a
Al
b
Fe
c
Ca
d

Figure 5

F5

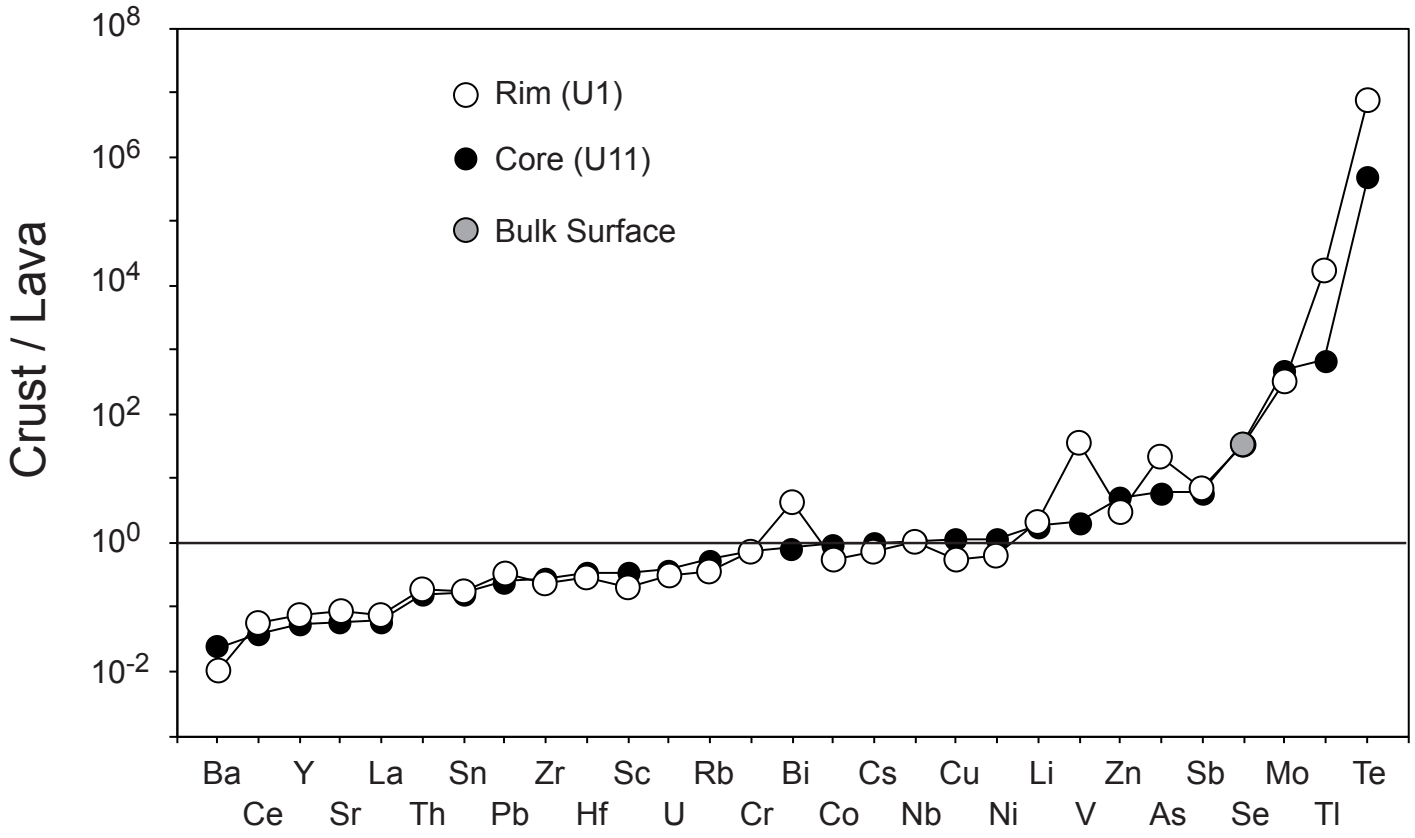
Crust / Lava
10^8
10^6
10^4
10^2
10^0
10^{-2}
Rim (U1)
Core (U11)
Bulk Surface
Ba Ce Y Sr La Th Sn Pb Zr Hf Sc U Rb Cr Bi Co Cs Nb Cu Ni Li V Zn As Sb Se Mo Tl Te

Figure 6

F6

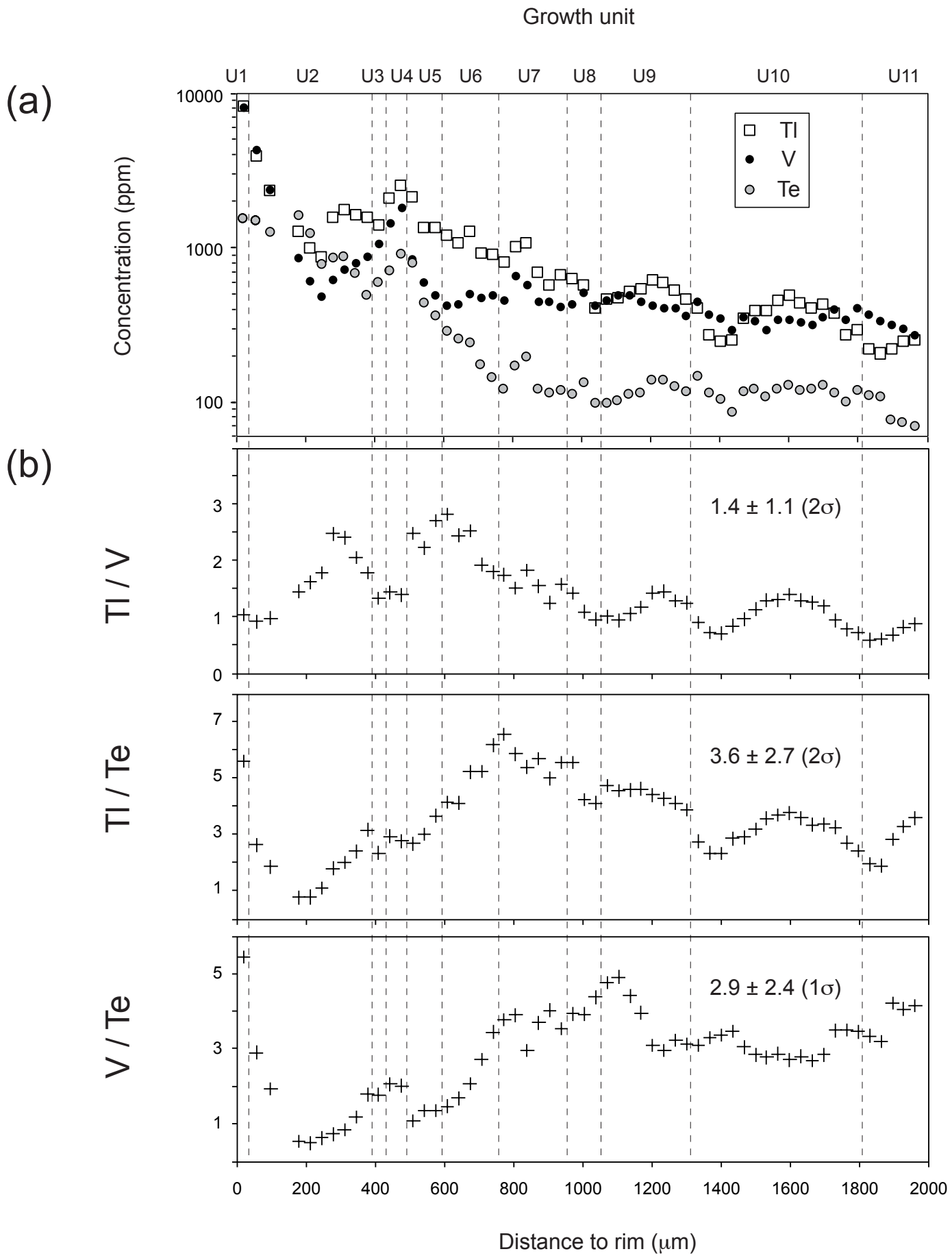
Growth unit
U1
U2
U3
U4
U5
U6
U7
U8
U9
U10
U11
(a)
Concentration (ppm)
10000
1000
100
Tl
V
Te
(b)
Tl / V
1.4 ± 1.1 (2σ)
Tl / Te
3.6 ± 2.7 (2σ)
V / Te
2.9 ± 2.4 (1σ)
0
200
400
600
800
1000
1200
1400
1600
1800
2000
Distance to rim (μm)

Figure 7

F7

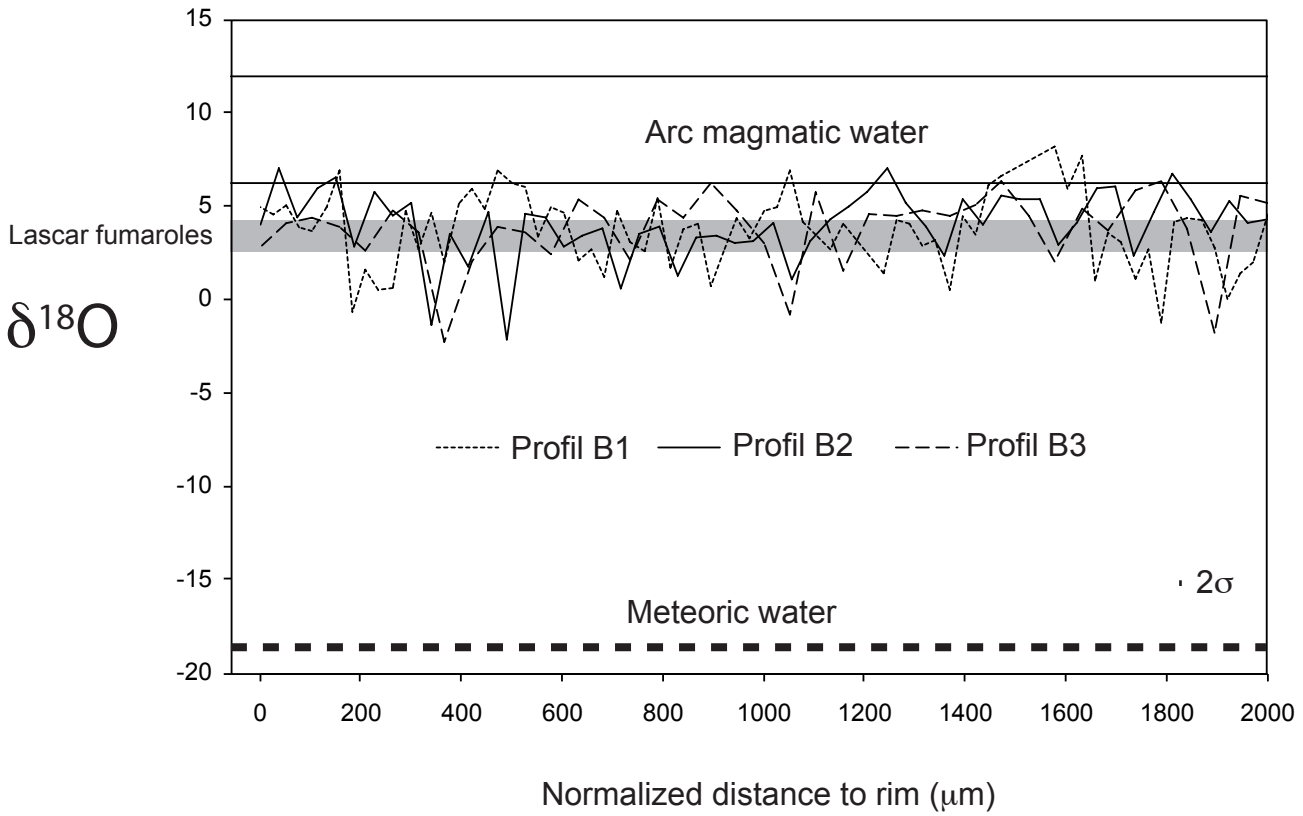
15
10
5
0
-5
-10
-15
-20
Arc magmatic water
Lascar fumaroles
δ18O
Profil B1
Profil B2
Profil B3
2σ
Meteoric water
0
200
400
600
800
1000
1200
1400
1600
1800
2000
Normalized distance to rim (μm)

Figure 8

F8

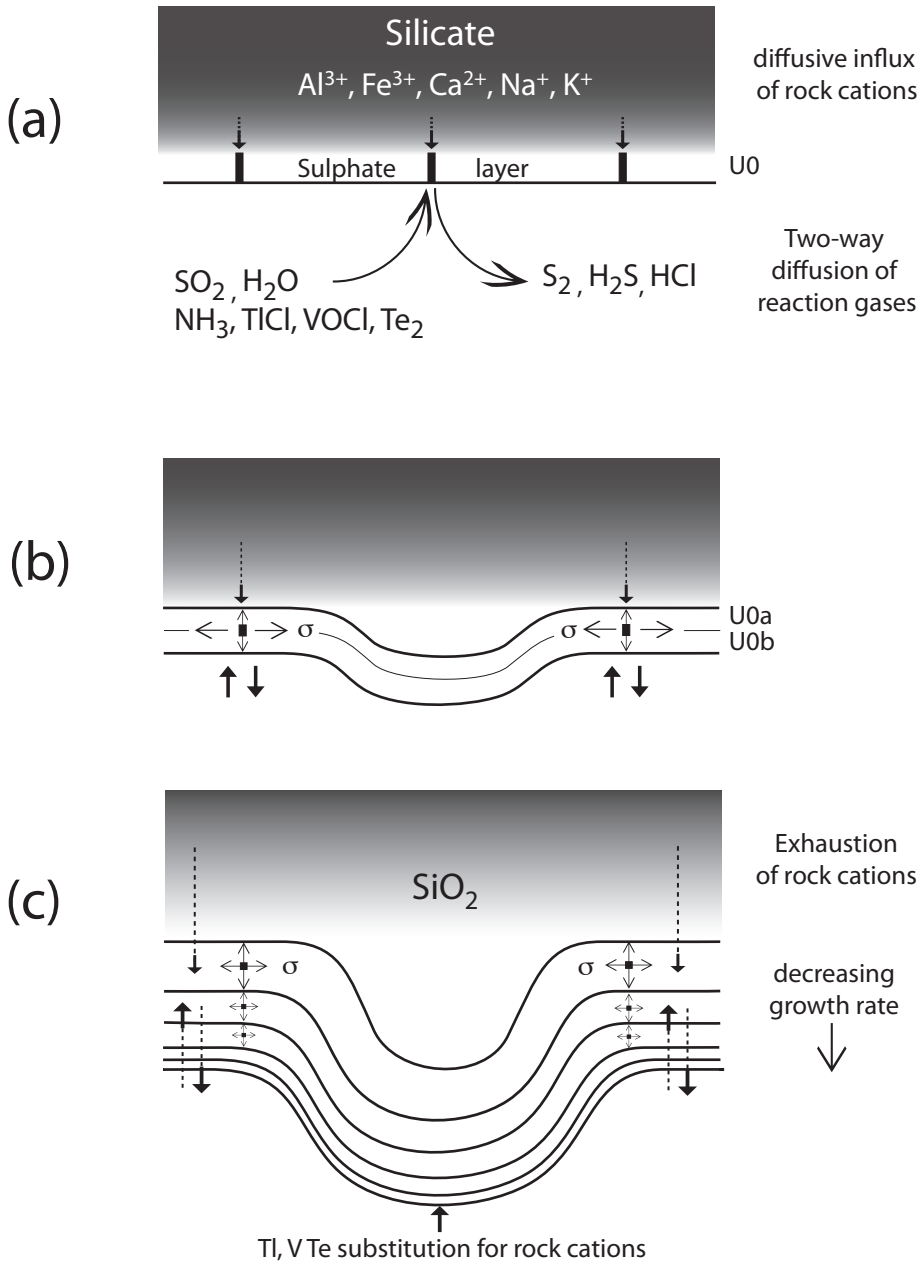
(a)
Silicate
Al^{3+}, Fe^{3+}, Ca^{2+}, Na^{+}, K^{+}
diffusive influx of rock cations
Sulphate layer
U0
SO_2, H_2O
NH_3, TlCl, VOCl, Te_2
S_2, H_2S, HCl
Two-way diffusion of reaction gases
(b)
σ
σ
U0a
U0b
(c)
SiO_2
Exhaustion of rock cations
σ
σ
decreasing growth rate
Tl, V Te substitution for rock cations

Figure 9

F9

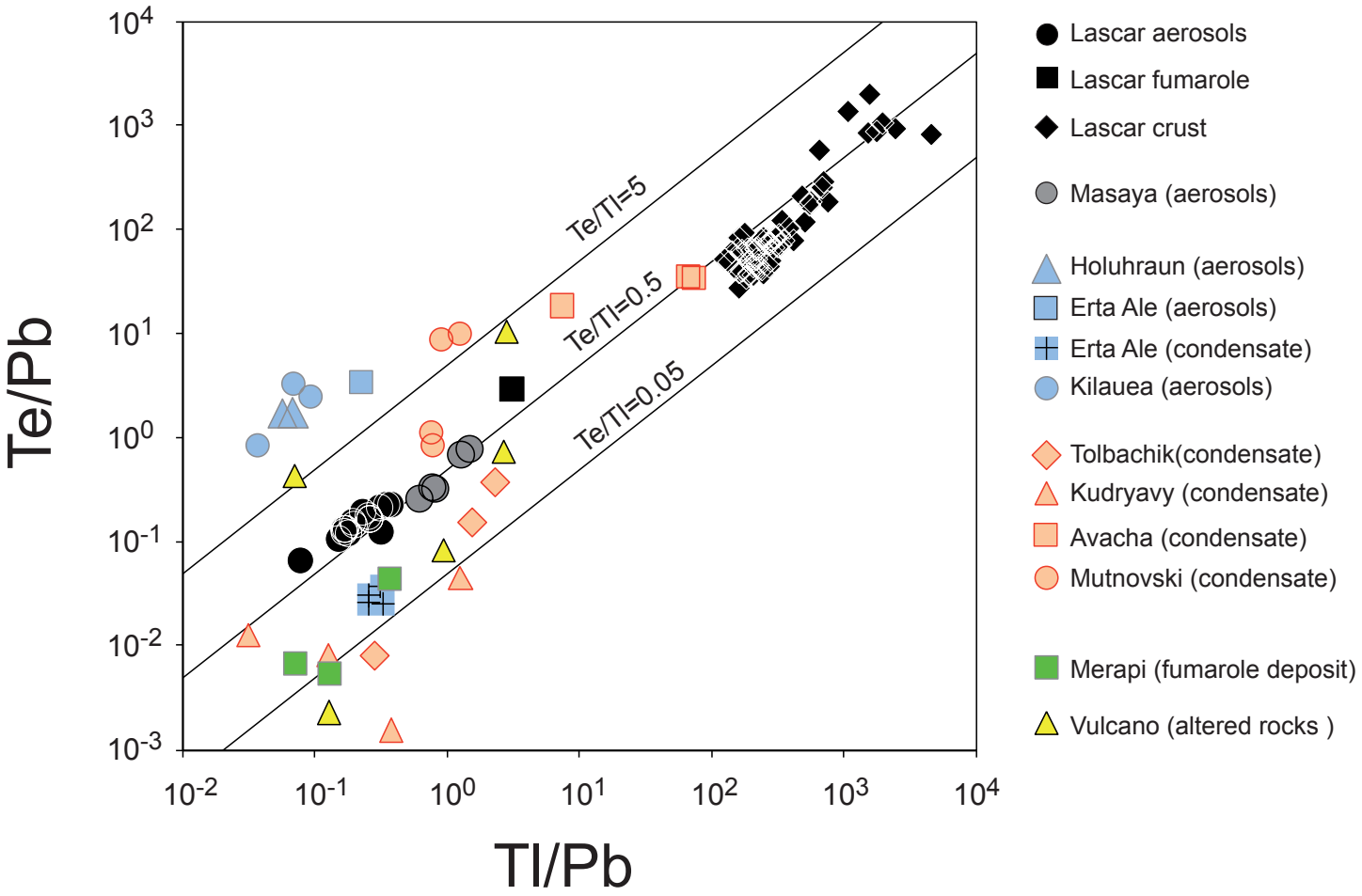
Te/Pb
Tl/Pb
Te/Tl=5
Te/Tl=0.5
Te/Tl=0.05
Lascar aerosols
Lascar fumarole
Lascar crust
Masaya (aerosols)
Holuhraun (aerosols)
Erta Ale (aerosols)
Erta Ale (condensate)
Kilauea (aerosols)
Tolbachik(condensate)
Kudryavy (condensate)
Avacha (condensate)
Mutnovski (condensate)
Merapi (fumarole deposit)
Vulcano (altered rocks)

Figure 10

F10

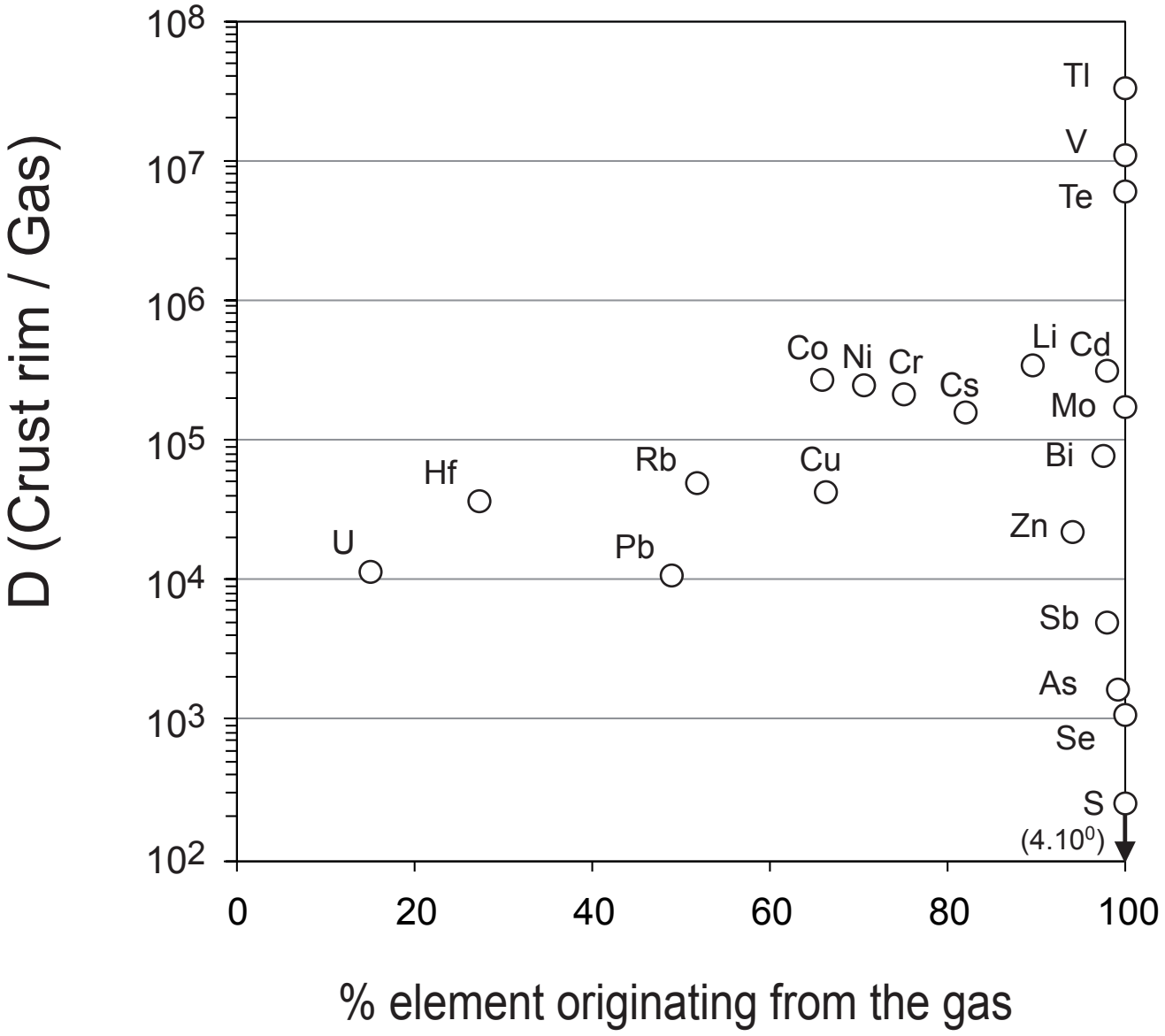

Figure 11

F11